The Astrophysical Journal, 965:16 (18pp), 2024 April 10 https://doi.org/10.3847/1538-4357/ad25f4

Inferring Fundamental Properties of the Flare Current Sheet Using Flare Ribbons: Oscillations in the Reconnection Flux Rates

Marcel F. Corchado Albelo[1,2,5], Maria D. Kazachenko[1,2], and Benjamin J. Lynch[3,4]
[1] Department of Astrophysical and Planetary Sciences, University of Colorado Boulder, 2000 Colorado Avenue, Boulder, CO 80305, USA; marcel.corchado@colorado.edu
[2] National Solar Observatory, 3665 Discovery Drive, Boulder, CO 80303, USA
[3] Space Sciences Laboratory, University of California, Berkeley, CA 94720, USA
[4] Department of Earth, Planetary, and Space Sciences, University of California, Los Angeles, CA 90095, USA
Received 2023 December 20; revised 2024 February 1; accepted 2024 February 1; published 2024 April 1

Abstract

Magnetic reconnection is understood to be the main physical process that facilitates the transformation of magnetic energy into heat, motion, and particle acceleration during solar eruptions. Yet, observational constraints on reconnection region properties and dynamics are limited due to a lack of high-cadence and high-spatial-resolution observations. By studying the evolution and morphology of postreconnected field-lines footpoints, or flare ribbons and vector photospheric magnetic field, we estimate the magnetic reconnection flux and its rate of change with time to study the flare reconnection process and dynamics of the current sheet above. We compare high-resolution imaging data to study the evolution of the fine structure in flare ribbons as ribbons spread away from the polarity inversion line. Using data from two illustrative events (one M- and X-class flare), we explore the relationship between the ribbon-front fine structure and the temporal development of bursts in the reconnection region. Additionally, we use the `RibbonDB` database to perform statistical analysis of 73 (C- to X-class) flares and identify quasiperiodic pulsation (QPP) properties using the Wavelet Transform. Our main finding is the discovery of QPP signatures in the derived magnetic reconnection rates in both example events and the large flare sample. We find that the oscillation periods range from 1 to 4 minutes. Furthermore, we find nearly cotemporal bursts in Hard X-ray (HXR) emission profiles. We discuss how dynamical processes in the current sheet involving plasmoids can explain the nearly cotemporal signatures of quasiperiodicity in the reconnection rates and HXR emission.

Unified Astronomy Thesaurus concepts: Solar flares (1496); Solar x-ray flares (1816); Solar magnetic reconnection (1504); Solar magnetic fields (1503); Solar physics (1476); Solar active region magnetic fields (1975)

1. Introduction

Solar flares are intense localized emission of light in the solar atmosphere that cover the full electromagnetic spectrum from radio to γ-rays (see review by Benz 2017). They are understood to be associated with the release of free magnetic energy stored in the twisted and sheared coronal magnetic fields via magnetic reconnection (see reviews by Priest & Forbes 2002; Hudson 2011; Shibata & Magara 2011). Although there is no direct measurement of the coronal magnetic reconnection, indirect observations, and models have helped to gain an understanding of this process.

The CSHKP, or a standard two-ribbon flare model named after Carmichael (1964), Sturrock (1966), Hirayama (1974), and Kopp & Pneuman (1976), explains many features in observations and numerical experiments. For example, it describes a sequence of coronal (flare) loops formed by reconnection as the magnetic reconnection point (so-called X-point in 2D) moves upward beneath an erupting flux rope (EFR; O-point in 2D) that is a coronal mass ejection (CME). These loops are anchored in opposite magnetic polarities, and the line separating these is referred to as the polarity inversion line (PIL). Nonthermal particles accelerated directly or indirectly during the reconnection process precipitate down the newly formed flare loops and arrive at the chromosphere. At the chromosphere, the density is high enough for the accelerated electrons and ions to deposit energy through bremsstrahlung and produce electromagnetic radiation at various wavelengths (e.g., H_α, ultraviolet, hard X-rays, γ-rays; Brown 1971). As the new flaring loops move higher into the corona, the location of the energy deposition moves away from the PIL. As the chromosphere is locally heated by condensed nonthermal particles, thermal conduction forces chromospheric material to rise (so-called chromospheric evaporation) and fill the newly reconnected flare loops, generating emission in soft X-rays (SXR) within the flare arcade. Understanding of the observed phenomena described above critically depends on our understanding of the details of magnetic reconnection.

Magnetic reconnection can proceed through different mechanisms that will dictate the rate through which new field lines are reconfigured. The simplest magnetic reconnection mechanism to explain the speed at which antiparallel magnetic field lines enter the reconnection site and have their magnetic topologies changed is the Sweet–Parker (SP) mechanism (Parker 1957; Sweet 1958a, 1958b; Parker 1963). This mechanism treats a single laminar layer current sheet stretching along the full interface between the opposing magnetic fields. The interface region is surrounded by plasma in ideal magnetohydrodynamic (MHD) conditions. This leads to a slow reconnection rate, or inflow speed of new field lines to the

[5] DKIST Ambassador.

reconnection site, of field lines $M_A = \frac{V_R}{V_A} = S^{-1/2}$, where $S = LV_A/\eta$ is the Lundquist number, η is the plasma resistivity, L the characteristic length of the system, and V_A is the Alfvén speed. This dependence on the Lundquist number yields a reconnection rate that is too slow to explain the energy release time during solar flares. The required inflow velocity for solar flares is on the order of tenths or hundredths of the Alfvén speed and is called fast reconnection. This requires that the reconnection rate has a weaker scaling dependence with the Lundquist number (Pucci et al. 2017). One alternative mechanism to explain fast reconnection is the Petschek model (Petschek 1964). The Petschek model assumes a smaller reconnection site compared to the current sheet length. This geometry creates a larger opening on the reconnection exhaust, which increases the outflow velocity of the newly formed magnetic fields. Another mechanism for fast reconnection is the Hall MHD, in which the current sheet is required to have a width of the ion inertial length. Lastly, another possibility of fast reconnection is through impulsive or bursty reconnection. Such a process requires an elongated SP-like current sheet undergoing a tearing instability. For a detailed review of magnetic reconnection mechanisms and their application to solar flares, see Pontin & Priest (2022) and Ji et al. (2022).

Tearing instability (TI) is when the CS becomes unstable and tears, breaks, and subsequently forms magnetic island plasmoids within the current layer (Furth et al. 1963; Shibata & Tanuma 2001). Shibata & Tanuma (2001) showed a scenario of cascading reconnection that results in bursty reconnection episodes. In this scenario, initially the CS is stretched out, and then the TI mode sets and fragments the CS, which forms multiple plasmoids. The plasmoids separate as they outflow toward the CS exhausts and trigger secondary and higher levels of TI, which we refer to as the plasmoid instability (PI) in order to account for the interactions and dynamics of the plasmoid structures (i.e., the effect of the TI on the further evolution of the magnetic reconnection process in the system). The higher level TI can continue forming plasmoids of smaller sizes until reaching the kinetic scale. This scenario has been supported both analytically (Loureiro et al. 2007; Uzdensky et al. 2010) and with numerical simulations (e.g., Forbes & Isenberg 1991; Karpen et al. 1998, 2012; Bhattacharjee et al. 2009; Lin et al. 2009; Samtaney et al. 2009; Huang & Bhattacharjee 2010; Bárta et al. 2011; Shen et al. 2011; Mei et al. 2012; Ni et al. 2015; Huang & Bhattacharjee 2016; Lynch et al. 2016; Mei et al. 2017; Li et al. 2019; Wang et al. 2022). Yet, with no clear observations of the coronal magnetic field in the reconnection site and limited temporal and spatial cadence, it is hard to directly observe these structures and their dynamics in the flare current sheets.

There is observational evidence showing blob-like structures propagating within current sheets in EUV, SXR, and radio observations, which have been interpreted as plasmoid structures within the current sheet (e.g., Ohyama & Shibata 1998; Kliem et al. 2000; Takasao et al. 2012; Hayes et al. 2019; Lu et al. 2022). These observations support the existence of plasmoids in the flare current sheet and that the TI and PI are present during flares. The plasmoids are usually observed as enhanced emission blobs or dark voids (depending on the energy range), propagating downward and upward along the current sheet. Studying these structures has allowed estimation of the reconnection properties of the CS, like the outflow speed of magnetic reconnection (Takasao et al. 2012; Lu et al. 2022), and provide links to quasiperiodic pulsations in flare lightcurves (Hayes et al. 2019).

Flare ribbons are localized enhancements of emission in the upper chromosphere (some 2000 km above the solar surface). The flare ribbons are usually observed in H_α and 1600 Å ultraviolet (UV) emission. They are interpreted as the signature of nonthermal particles precipitating from a coronal source due to magnetic reconnection into the dense chromosphere marking the footpoints of newly reconnected flare loops (Forbes 2000; Fletcher et al. 2011; Qiu et al. 2012; Li et al. 2014, 2017; Longcope 2014; Graham & Cauzzi 2015; Priest & Longcope 2017). As such, they provide a powerful tool to indirectly observe and diagnose the current sheet properties during magnetic reconnection.

Forbes & Priest (1984) and Forbes & Lin (2000) described the quantitative relationship between the reconnected flux rate and the motion of the flare ribbons within the CSHKP model. They used the rate of photospheric magnetic flux change $\dot{\Phi}_{\rm phot}$ swept by the flare ribbons to determine the magnetic reconnection rate, i.e., the rate at which the coronal magnetic flux is processed through the current sheet in 3D:

$$\frac{\partial \Phi_{\rm c}}{\partial t} = \frac{\partial}{\partial t}\int B_{\rm c} dS_{\rm c} = \frac{\partial}{\partial t}\int B_{\rm n} dS_{\rm rbn} = \frac{\partial \Phi_{\rm phot}}{\partial t}. \quad (1)$$

Here the coronal magnetic field $B_{\rm c}$ reconnection rate $\frac{\partial \Phi_{\rm c}}{\partial t}$ is defined by the integration of an inflow coronal magnetic field over the reconnection area $dS_{\rm c}$. Unfortunately, this quantity is not readily available from observations due to difficulties in measuring the coronal magnetic field and the resolution needed to resolve the reconnection site area. However, by conservation of magnetic flux we can use the change per unit time of flare ribbon magnetic flux $\frac{\partial \Phi_{\rm phot}}{\partial t}$ to infer the change of the coronal field during magnetic reconnection. In the expression above, the magnetic flux Φ or $\Phi_{\rm phot} = \int B_{\rm n} dS_{\rm rbn}$, $B_{\rm n}$ is the normal component of the photospheric magnetic field, and $dS_{\rm rbn}$ is the area swept by the flare ribbon. Measurements of the flare ribbon magnetic flux are relatively straightforward with current observation capabilities. This allows the creation of databases like the `RibbonDB` (Kazachenko et al. 2017), which contains reconnection fluxes and other related properties for more than 3000 flares.

High-resolution observations of swirls and wave breaks in flare ribbons and the ribbon fronts (newly brightened kernels in the chromosphere) suggest that flare ribbon evolution is connected to current sheet processes. Particularly, the flare ribbon structure has been linked to wave-generating processes at the flare loop tops (Brannon et al. 2015) and to the existence of plasmoid structures within the current sheet (see French et al. 2021; Wyper & Pontin 2021; Naus et al. 2022 and Section 2.2 of the review by Kazachenko et al. 2022). Therefore, high-cadence and high-spatial-resolution studies of flare ribbons and their comparison with numerical flare models could potentially tell us about the physics of the current sheet and magnetic reconnection during flares, providing the missing link between the reconnection properties and other flare phenomena like particle acceleration. Particle-in-cell (PIC) models have shown that contracting magnetic islands can also accelerate particles trapped within them (Drake et al. 2006; Guidoni et al. 2016). Recent theoretical work has shown that nonthermal particle populations traveling through consecutive magnetic islands can

give rise to a population of particles capable of producing the typical SXR and hard X-ray (HXR) emission observed during flares (Guidoni et al. 2022). They also provide a possible mechanism to explain particle acceleration contained within confined temporal enhancements or bursts, which might show periodic, oscillatory, or intermittent behavior.

Observations of solar and stellar flare lightcurves in multiple frequencies have shown oscillatory contributions usually referred to as quasiperiodic pulsation (QPPs; see reviews by Nakariakov & Melnikov 2009; Van Doorsselaere et al. 2016). Their existence within the whole spectrum of flare emission suggests that multiple mechanisms might be causing oscillatory and bursty particle acceleration (see review by McLaughlin et al. 2018), including MHD waves (Thurgood et al. 2017), plasmoid interactions with the flaring loops and among themselves (Kliem et al. 2000; Barta et al. 2008; Jelínek et al. 2017), and existence of termination shocks due to the superposition of reconnection outflow jets (Takahashi et al. 2017). Therefore, observational constraints could help our understanding of the mechanism behind these QPPs, which in turn could improve our modeling capabilities of solar and stellar flares.

In this paper, we report the observations of oscillation in the magnetic reconnection rates of dozens of flares. To our knowledge, it is the largest survey to date. Specifically, we present a statistical analysis of 73 events from the `RibbonDB` database, which has cotemporal HXR and SXR observations. From our analysis, we provide an observational reference relating oscillations in reconnection rates with particle acceleration proxies in HXR and SXR with the goal of understanding the details of the flare reconnection process and its relationship with particle acceleration. The structure of the paper is as follows. In Section 2 we describe the data we used in this study, the methods used to derive the magnetic reconnection properties from flare ribbon and magnetogram observations, and the detection algorithm we used to identify the QPPs. In Section 3 we first show examples of individual flares, comparing spatial flare ribbon evolution to the evolution of the reconnection budget and the rate of its change with time; we then compare oscillating reconnection flux/rate evolution with cotemporal SXR and HXR emissions and summarize the results of the 73 events. In Section 4 we discuss and interpret our results in the context of recent works in the field. Finally, we summarize our findings in Section 5.

2. Data and Methods

2.1. Data Description

In this section we describe the observations from the Helioseismic Magnetic Imager (HMI) and Atmospheric Image Assembly (AIA) on board the Solar Dynamics Observatory (SDO), Interface Region Imaging Spectrograph (IRIS), Fermi Gamma-ray Space Telescope (Fermi), and Geostationary Operational Environmental Satellite (GOES), the methodology for evaluating magnetic reconnection flux and and its rate and our analysis of the QPPs using the Wavelet Transform.

2.1.1. SDO: AIA and HMI

We use the data from SDO (Pesnell et al. 2012) to derive flare ribbons' spatial properties and reconnection fluxes/rates. SDO provides the capability to derive high-quality spatial and temporal observations of the full-disk intensity maps in different narrowband filters and vector magnetic fields on the same platform, allowing the cospatial observations of flare ribbons and their host active region's photospheric magnetic fields. AIA (Lemen et al. 2012) observes in seven extreme ultraviolet (EUV) and three UV channels. For the purpose of this study, we use the 1600 Å intensity maps, corresponding to a characteristic temperature response of 10^5 and 5000 K, sensitive to chromospheric emissions. The spatial resolution is $0\farcs6$, and the cadence is 24 s. HMI provides the photospheric magnetic field strength, inclination, and azimuth (Hoeksema et al. 2014), which can be transformed into B_x, B_y, and B_z (Sun 2013; Bobra et al. 2021). To improve the quality of the signal, vector-field frames produced every 135 s were combined into a 720 s cadence observable, with a pixel resolution of $0\farcs5$.

2.1.2. IRIS: SJI Images

For inferring the fine structure of flare ribbons, we use observations from IRIS (De Pontieu et al. 2014, 2021). IRIS observes in far ultraviolet (FUV) and near ultraviolet (NUV) passbands since 2013 June. The satellite has two science instruments, a Spectrograph (SG) and a Slit-Jaw Imager (SJI). The SG has a field of view (FOV) up to 175″ and a spatial resolution of $0\farcs33$–$0\farcs4$ for FUV and NUV, respectively. It probes a wide temperature regime from the photosphere (5000 K) to the corona (10^6–10^7 K), looking at FUV (1332 Å–1358 Å and 1389 Å–1407 Å), and NUV (2783 Å–2835 Å) lines. The SJI observes with a ranging cadence on the order of seconds with a spatial resolution of usually $0\farcs166$ covering a FOV of up to 175″ ×175″, in four passbands probing the transition region (C II 1335 Å and Si IV 1400 Å), chromosphere (Mg II k 2796 Å), and photosphere (continuum 2830 Å). To extract and use the IRIS level 2 data, which have been corrected for flat field, dark currents, systematic offsets, and geometric correction with the IDL script *iris_prep.pro* (De Pontieu et al. 2021), we use the *sunkit-instruments* package from the Python library (Barnes et al. 2020).

2.1.3. Fermi: GBM

To describe high-energy flare properties, we use observations from Fermi (Atwood et al. 2009). Fermi has two instruments, the Large Area Telescope (LAT) and the Gamma-ray Burst Monitor (GBM, Meegan et al. 2009). These instruments are used to observe high-energy astrophysical phenomena: high-energy γ-ray blazars, pulsars, γ-ray bursts, high-energy solar flares, etc. The LAT, serving as the primary instrument on board Fermi, is a wide field-of-view imager covering an energy range of ≈20 MeV to ≈300 GeV. The GBM expands the LAT capabilities to energy ranges below those observed by LAT into the HXR range. The GBM produces three data types, out of which two are temporally binned—Continuous Time (CTIME) and Continuous Spectroscopy (CSPEC), and Time-Tagged Events (TTE). For large solar flares, TTE data is usually lost, and thus CTIME and CSPEC are the best data products used to evaluate temporal and spectral evolution during flares. We use the OSPEX IDL software[6] to download CSPEC data, which has a varying cadence from 1.0 to 32.7 s, and the default value of 4.0 s stored in 128 quasi-logarithmic energy bins, which can be integrated

[6] https://hesperia.gsfc.nasa.gov/fermi_solar/analyzing_fermi_gbm.htm

into the following energy channels of interest: 8–15, 15–25, 25–50, 50–100, and 100–300 keV.

2.1.4. GOES: XRS

Finally, to describe flare lightcurves in soft X-ray (SXR) we use observations from GOES (Bornmann et al. 1996; Chamberlin et al. 2009; Machol et al. 2019). GOES includes several geosynchronous spacecraft flown by the National Oceanic and Atmospheric Administration (NOAA) since 1974. Their main application has been to observe the terrestrial weather and monitor many aspects of the space environment. The solar X-ray Sensor (XRS) measures an incoming solar X-ray emission with a cadence of 1 s in two channels, 0.5–4 Å and 1–8 Å, corresponding to an energy range of ≈1.5 to ≈25 keV.

2.2. Methodology

In this section we first describe the selection criteria for the 73 flares in this study. We then describe how we use AIA full disk 1600 Å, and IRIS SJI 1330 Å and 1400 Å images to create masks of the flaring ribbon area and calculate the reconnection flux and its rate for each flare in our sample, including their uncertainties. Finally, we present the Wavelet Transform analysis (Torrence & Compo 1998; Auchère et al. 2016) used to characterize and identify the most significant oscillating modes/frequencies for different time series in our data.

2.2.1. Data Selection

We select 73 flares from the `RibbonDB` database (Kazachenko et al. 2017) of various flare classes: 10 X-class, 24 M-class, and 39 C-class flares observed from 2010 to 2016. These events are selected manually and represent a subsample from more than 3000 flares in the `RibbonDB` database. We only selected events that exhibit oscillations in magnetic reconnection rates and have cotemporal X-ray emission time series observations from both GOES XRS and Fermi GBM instruments. Specifically, we compare three time series: magnetic reconnection flux/rate proxies, SXR emission and its rate (0.5–4 Å and 1–8 Å), and HXR emission (8–15, 15–25, 25–50, 50–100, and 100–300 keV).

In addition, for eight events for which there were cotemporal and cospatial IRIS and SDO observations, we used IRIS SJI observations to examine fine structure in flare ribbon fronts. While these observations have 1.82–3.75 times higher spatial resolution than the AIA observations, they have limited FOV, often missing the full extension of the flare ribbons observed by AIA. We therefore only use IRIS data to identify the fine-structure development for eight out of 73 events included in this study, and not the reconnection flux analysis.

2.2.2. Estimating Magnetic Reconnection Flux and Reconnection Flux Rates

To identify the reconnection flux $\Phi(t)$, we use the vertical component of the HMI vector magnetic field maps and AIA 1600 Å ribbon maps. To identify the ribbon area $A_{\rm rbn}(\boldsymbol{x}, t; c)$, we use the procedure described in Kazachenko et al. (2017), for AIA and IRIS SJI images. Then the reconnection flux

$$\Phi^{(I_c)}(t_k) = \int dA_{\rm rbn}(\boldsymbol{x}, t_k; c) B_n(\boldsymbol{x}, t_k) \approx \sum_i^{N_i}\sum_j^{N_j} \mathcal{M}^{(I_c)}(x_i, y_j, t_k) B_r(x_i, y_j, t_k)\Delta A. \quad (2)$$

The numerical approximation of the magnetic reconnection flux at a time t_k is defined as $\Phi(t_k)$. In this numerical approximation $\mathcal{M}^{(I_c)}(x_i, y_j, t_k)$ refers to the cumulative mask at a time t_k of the sequence of AIA or IRIS SJI images, x_i and y_j refer to the horizontal position of a given pixel, ΔA refers to the pixel area size, and I_c to the cutoff intensity criteria to identify the flare ribbon pixels. The cumulative mask—$\mathcal{M}^{(I_c)}(x_i, y_j, t_k) = \mathcal{M}^{(I_c)}(x_i, y_j, t_{k-1}) \bigcup \mathcal{N}^{(I_c)}(x_i, y_j, t_k)$—is defined as the set of all the flaring pixels in the instantaneous mask $\mathcal{N}^{(I_c)}(x_i, y_j, t_k) \in I \geqslant I_c$ up to the kth image in the sequence of observations. The IRIS SJI and HMI observations are coaligned. Since the IRIS SJIs have higher spatial resolution than the HMI maps, we use *SunPy* to reproject the HMI data to match the dimensions of the IRIS SJI.

We use a cumulative flare ribbon mask to account for the dynamic lifetime of individual flaring pixels. Thus, once a pixel has brightened up and satisfies $I(x_i, y_j, t_k) > I_c(t_k)$, it is included as part of the flare ribbon mask until the end of the event. The cutoff intensity, which determines if a bright pixel belongs to the instantaneous flare ribbon mask, is defined as $I_c(t_k) = \text{median}(I(x_i, y_j, t_k)) \cdot c$. We use the median as it measures the central value of the intensity maps with a lower bias to the flaring pixels, as compared to the mean intensity. The median intensity of each map is used as a proxy for the intensity of the background chromospheric emission. We use the cutoff parameter $c = \{6, 10\}$, obtained from empirical results both using the 1600 Å AIA, and 1330 Å and 1400 Å IRIS SJI intensity maps. With this range of cutoff intensities, we define the positive and negative reconnection fluxes and the errors in these estimates for positive (+) and negative (−) polarities, respectively:

$$\Phi^{\pm}(t_k) = \frac{\Phi^{\pm}I_6(k) + \Phi^{\pm}I_{10}(t_k)}{2}. \quad (3)$$

$$\delta\Phi^{\pm}(t_k) = \frac{|\Phi^{\pm}I_{10}(t_k) - \Phi^{\pm}I_6(t_k)|}{2}. \quad (4)$$

The reconnection flux rate for each magnetic polarity is then defined as the time derivative of the reconnection flux $\dot{\Phi}^{\pm}(t_k) = \frac{\Phi^{\pm}(t_{k+1}) - \Phi^{\pm}(t_{k-1})}{t_{k+1} - t_{k-1}}$. The uncertainty in the reconnection rate for any given time can be estimated using the same formalism as for the reconnection flux:

$$\delta\dot{\Phi}^{\pm}(t_k) = \frac{|\dot{\Phi}^{\pm}I_{10}(t_k) - \dot{\Phi}^{\pm}I_6(t_k)|}{2}. \quad (5)$$

Finally, for a clearer comparison of the magnetic reconnection flux and its rate derived from the flare ribbons with the observed SXR and HXR emission, we quantify the unsigned reconnection flux and its rate, including uncertainty estimates. First, we define both the unsigned reconnection fluxes and rates as the average between the absolute values of the positive and negative quantities:

$$\Phi(t_k) = \frac{\Phi^{+}(t_k) + |\Phi^{-}(t_k)|}{2}, \quad (6)$$

$$\dot{\Phi}(t_k) = \frac{\dot{\Phi}^+(t_k) + |\dot{\Phi}^-(t_k)|}{2}. \quad (7)$$

We then define the uncertainty of these measurements as the absolute value of the difference between the two:

$$\delta\Phi(t_k) = \frac{|\Phi^+(t_k) - |\Phi^-(t_k)||}{2}, \quad (8)$$

$$\delta\dot{\Phi}(t_k) = \frac{|\dot{\Phi}^+(t_k) - |\dot{\Phi}^-(t_k)||}{2}. \quad (9)$$

In this approach, the uncertainty of the unsigned fluxes and rates captures the discrepancy between reconnection fluxes and rates at any given time between the opposite magnetic polarities. Ideally, the values of the reconnection flux and their rates should be equal through the full flare evolution since they correspond to the same flaring loop system. The offset represents the uncertainty contributions from the flare ribbon masking algorithm and the vector magnetic field observations.

2.2.3. Quantifying Quasiperiodic Pulsations

Similar to other astrophysical processes (e.g., Aschwanden 2011), the Fourier power spectrum of the magnetic reconnection rates follows a power law distribution with frequency, which makes identifying modes of oscillation from the Fourier power spectrum complicated. Further complication arises due to nonstationary oscillations, oscillations with period drifts, which are not accurately described with Fourier Transform methods (e.g., Inglis et al. 2015, 2016). Thus, to accurately describe a flare oscillation, we need a method that can identify the distribution of power among oscillatory modes and how they change over time. The Wavelet Transform accounts for both of these properties and thus is able to identify the most significant stationary and nonstationary oscillations in flare observations, making the Wavelet Transform suitable for studying the statistical properties of flare-related oscillations (Broomhall et al. 2019).

In this paper we use the Wavelet Transform analysis developed by Torrence & Compo (1998) and modified by Auchère et al. (2016). This method has been applied to detect QPPs in solar (Clarke et al. 2021; Kou et al. 2022) and stellar flares (López et al. 2019), space weather variability (Richardson & Cane 2010), astroseismology (Mathur et al. 2010), and Earth-climate variability (Webster et al. 1998; Moy et al. 2002). Below we present a brief summary of the Wavelet Transform analysis applied to flare time series $S(t_k)$:

1. Shift the mean of the original time series to zero and normalize it by the standard deviation $\hat{S}(t_k) = \frac{S(t_k) - \mu_S}{\sigma_S}$. Here $\hat{S}$ is the normalized time series, μ_S is the mean of the original time series, and σ_S is the variance of the original time series.
2. Apply the continuous Morlet Wavelet with a nondimensional frequency $\omega_0 = 6$, which is normalized at each frequency such that the energy is unity.
3. Calculate the regions of the Wavelet Spectrum affected by the finite-length, zero-padded boundaries, called the Cone-of-Influence (COI).
4. Model the background wavelet transform power and time-averaged wavelet power spectrum as colored noise following a power law distribution inside the COI.
5. Use this background spectrum to evaluate which signatures of the wavelet transform power, and the time-averaged wavelet power spectrum exceed the 95% significance level of not being attributed to colored noise.
6. Identify the period (the QPP period) in which the time-averaged wavelet power spectrum exceeding the 95% colored noise significance level has a local maxima.
7. Calculate the Fourier Power spectrum of the normalized time series and identify the period with the local maximum of Fourier power exceeding the 95% significance level of colored noise.
8. Repeat all of the above steps for the fluctuating component of the time series $\delta S(t_k) = S(t_k) - \bar{S}(t_k)$, where $\bar{S}(t_k)$ is the slow varying or background part of the time series. The background time series is calculated using a Savitzky–Golay filter with a 5 minute window.
9. Compare the QPP periods obtained from the original (S) and fluctuation (δS) time series.

3. Results

In this section we first show two illustrative examples of the spatiotemporal evolution of flare ribbons as observed with AIA 1600 Å, IRIS SJI 1330 Å, and 1400 Å. We then present the evolution of reconnection fluxes and their rates calculated using the HMI photospheric vector magnetograms and compare these with X-ray emission measured by Fermi and GOES. Specifically we compare the oscillation periods for each observation and the delay between the reconnection rate and X-ray emission oscillations. Finally, we present the results of our statistical analysis for 73 flares with cotemporal SDO, Fermi GBM, and GOES XRS observations.

3.1. Flare Case Studies with Coordinated SDO, IRIS, Fermi, and GOES Observations

3.1.1. Reconnection-rate Oscillations: X1.6 Flare in AR 12158

In the left panel of Figure 1 we show the spatiotemporal evolution of flare ribbons in an X1.6-class flare in AR 12158 observed for 1 hr on 2014 September 10 from 17:19 to 18:19 UTC. The cotemporal full-disk observation obtained from SDO allowed us to track the evolution of the flare ribbons as they swept the active region NOAA 12158. The vertical photospheric magnetic field shown in gray scale is saturated at ± 1000 G for each corresponding polarity. The top right panel of Figure 1 shows how the cumulative reconnection fluxes in positive and negative polarities increased to 6.54×10^{21} Mx and -5.65×10^{21} Mx, respectively. The bottom right panel in Figure 1 shows the evolution of the reconnection rate. The reconnection rates are maximum in each polarity, corresponding to 11.17×10^{18} Mx s^{-1} and -9.30×10^{18} Mx s^{-1}. As ribbons evolved, the reconnection rate exhibited a series of oscillations of similar magnitudes in both polarities. These bursts gradually decayed as the flare reached its end. We found that larger peaks in the reconnection rates occurred earlier in the flare at $t <$ 17:34 UTC (blue) when the flare ribbons swept the majority (>70%) of the reconnection flux. Finally, we estimated the unsigned reconnection flux within each burst as $\Phi_B(l) = \Phi(t_{l,\mathrm{end}}) - \Phi(t_{l,\mathrm{onset}})$, where $t_{l,\mathrm{onset}}$ and $t_{l,\mathrm{end}}$ are the onset and end times of each reconnection-rate burst l. We found that for this flare the distribution of

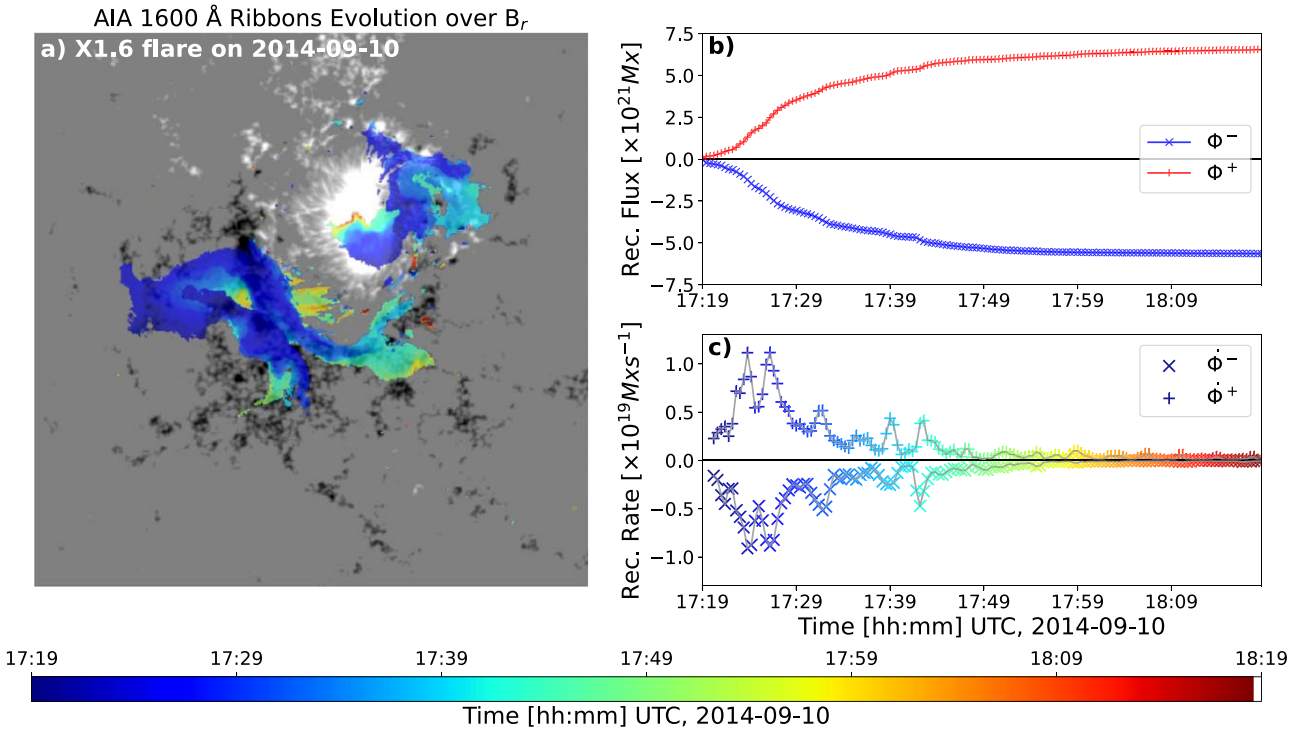

Figure 1. Evolution of flare ribbons and reconnection flux/rate during an X1.6 flare on 2014 September 10 using HMI and AIA 1600 Å observations. (a) Cumulative flare ribbon mask, colored from early evolution (blue) to the end of the flare (red), over the vertical magnetic field B_r in gray scale and saturated at ± 1000 G. (b) Reconnection flux proxy within positive (red +) and negative (blue -) polarity flare ribbons. (c) Reconnection rates for each of the flare ribbons corresponding to each magnetic polarity; the color corresponds to the flare ribbon cumulative mask evolution. See Section 3.1.1 for more details.

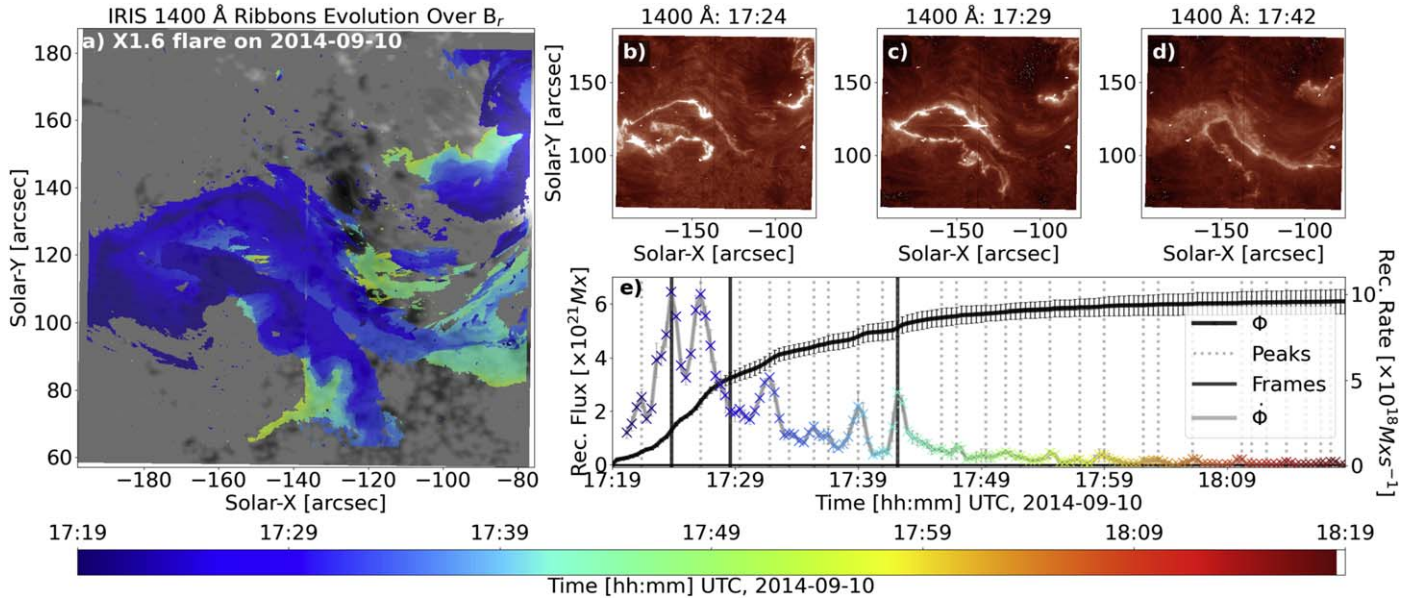

Figure 2. Evolution of flare ribbon fine structure during an X1.6 flare in AR 12158 (see also Figure 1) using IRIS 1400 Å SJI observations. (a) IRIS 1400 Å cumulative flare ribbon mask evolution over HMI B_r. (b) IRIS SJI observations of flare ribbons during the reconnection-rate maximum at $t \approx 17{:}24$ UTC. (c) Flare ribbons during the decay of the second largest reconnection-rate burst at $t \approx 17{:}29$ UTC. (d) Flare ribbons during a later reconnection-rate burst at $t \approx 17{:}32$ UTC. (e) Unsigned reconnection flux (black) and its rate (gray). The dotted vertical gray and solid vertical black lines represent the reconnection-rate peaks and the IRIS observation frames shown in panels (b)–(d), respectively. See Section 3.1.2 for more details.

reconnected fluxes in each burst ranges from 0.2×10^{20} Mx to 6×10^{20} Mx.

3.1.2. Fine Structure of Flare Ribbons: X1.6 and M3.7 Flares

Figure 1 illustrates how the evolution of the reconnection rate is strongly related to the motion of flare ribbons and ribbon spatial structure. To understand the details of the relationship between the flare ribbon spatial structure affecting the reconnection rates, we use high-resolution and high-cadence IRIS SJI observations. Specifically, we focus on understanding the connection between the flare ribbon fine structure, which we use to refer to the complexity in the form of waves and swirls on the ribbon fronts,

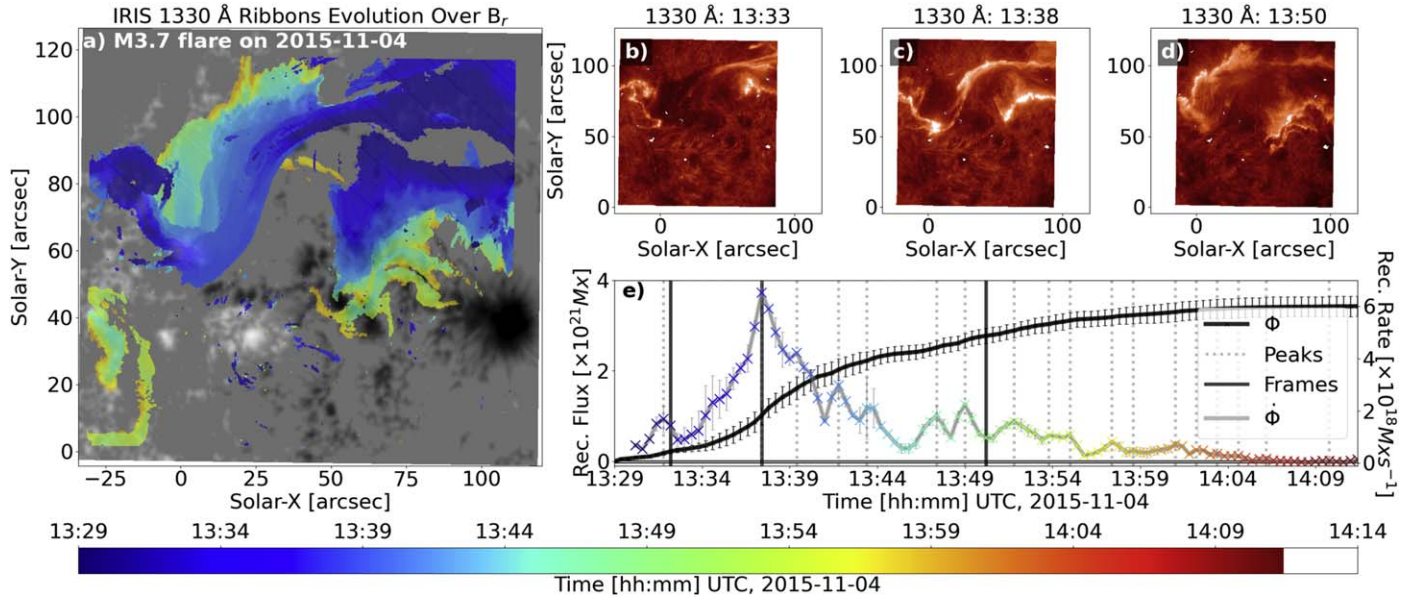

Figure 3. Evolution of flare ribbon fine structure during an M3.7 flare on 2015 November 4 in AR 12443 using IRIS 1330 Å SJI observations. (a) Cumulative flare ribbon mask evolution over B_r as in Figure 2. (b) Flare ribbons before the reconnection rate maximum $t \approx 01:33$ UTC. (c) Flare ribbons at the reconnection rate maximum $t \approx 01:38$ UTC. (d) Flare ribbons during the decay of a reconnection-rate burst at $t \approx 01:42$ UTC. (e) Unsigned reconnection flux and rate. See Section 3.1.2 for more details.

and the bursts in the reconnection rates. Figures 2(a) and 3(a) show the evolution of the cumulative flare ribbon mask derived from the IRIS SJI observations for the same X1.6 flare on 2014 September 10, as shown in Figure 1, and the M3.7 flare observed on 2015 November 4, respectively. The 2014 September 10 flare is observed in the 1400 Å filter with a spatial resolution of $0\farcs166 \times 0\farcs166$ and a 19 s cadence, while the 2015 November 4 flare is observed in the 1330 Å filter with a $0\farcs322 \times 0\farcs322$ resolution and a 12 s cadence. These high-resolution flare ribbon masks are compared to the average unsigned reconnection flux and its rate calculated using AIA 1600 Å observations.

First, we analyze the X1.6 flare described in Section 3.1.1. Figure 2 has a smaller FOV than the cutout from the full solar disk observations of SDO. This limits the use of the SJI observations to calculate the magnetic reconnection flux/rate since they rarely capture the full spatial evolution of flare ribbons. We therefore continue using AIA 1600 Å data to calculate our reconnection flux/rate proxies. Yet, the high-spatial-resolution SJI observations from IRIS show fine-structure details within the flare ribbon fronts. The SJIs in Figures 2((b)–(d)) highlight how the flare ribbon evolves in response to bursts in the reconnection rates. The SJIs display fine structure in the form of swirls and waves, which emerge and decay through the lifetime of the reconnection-rate bursts. These fine-structure patterns contribute to the large-scale bursty evolution of the flare ribbon, as ribbons sweep new magnetic flux from the active region. For the first time, we relate bursty sweeps in the spatial evolution of flare ribbons to bursts in the magnetic reconnection rate, which temporally evolve as quasiperiodic oscillations.

The cotemporal development of fine structure and quasiperiodic reconnection-rate burst is also observed in Figure 3 for the M3.7 flare on 2015 November 4. The ribbon masks derived from IRIS observations (Figure 3(a)) show that during the early stages of the flare ($t < 13:45$ UTC), the flare ribbon has swept more than 50% of the total reconnection flux in five reconnection-rate bursts. Similar to Figures 2((b)–(d)), the 1330 Å IRIS SJIs show the codevelopment of fine structure and reconnection-rate bursts. We also find that fluxes swept by individual bursts range from 0.5×10^{20} to 6.5×10^{20} Mx. The cotemporal development of flare ribbon fine structure, observed in 1330 Å and 1400 Å passbands, and the reconnection-rate QPPs suggests that these phenomena could be related to the dynamics of magnetic reconnection and conditions of the current sheet.

We propose that the fine-scale structures that are observed in the high-spatial-resolution IRIS SJI observations are related to processes and structures higher in the corona where magnetic reconnection with the flare loops is happening (i.e., the current sheet; Brannon et al. (2015), Wyper & Pontin (2021)). In Section 4 we compare this interpretation and others with our findings of magnetic reconnection-rate bursts in more detail.

3.1.3. Comparison of Fluctuations in the Reconnection Rate with Fluctuations in the X-Ray Flux: M3.7 and M2.1 Flares

Until now we have focused our attention on the spatial complexities of flare ribbons and their relationship with QPP bursts in the magnetic reconnection rates. In this section we compare the temporal evolution of the reconnection flux rate to the emission of HXR lightcurves. Specifically, we study two flares, the M3.7 flare on 2015 November 4 and the M2.1 flare on 2012 March 6.

In Figure 4 we show examples of X-ray lightcurves from Fermi GBM and GOES XRS for two flares (out of 73): an M3.7 flare on 2015 November 4 (also shown in Figure 3) and an M2.1 flare on 2012 March 6. We only include those Fermi channels that are not affected by noise and where observations from two GOES channels are available. We further use the derivative of the GOES SXR emission as a proxy for the HXR emission via the Neupert effect (Neupert 1968).

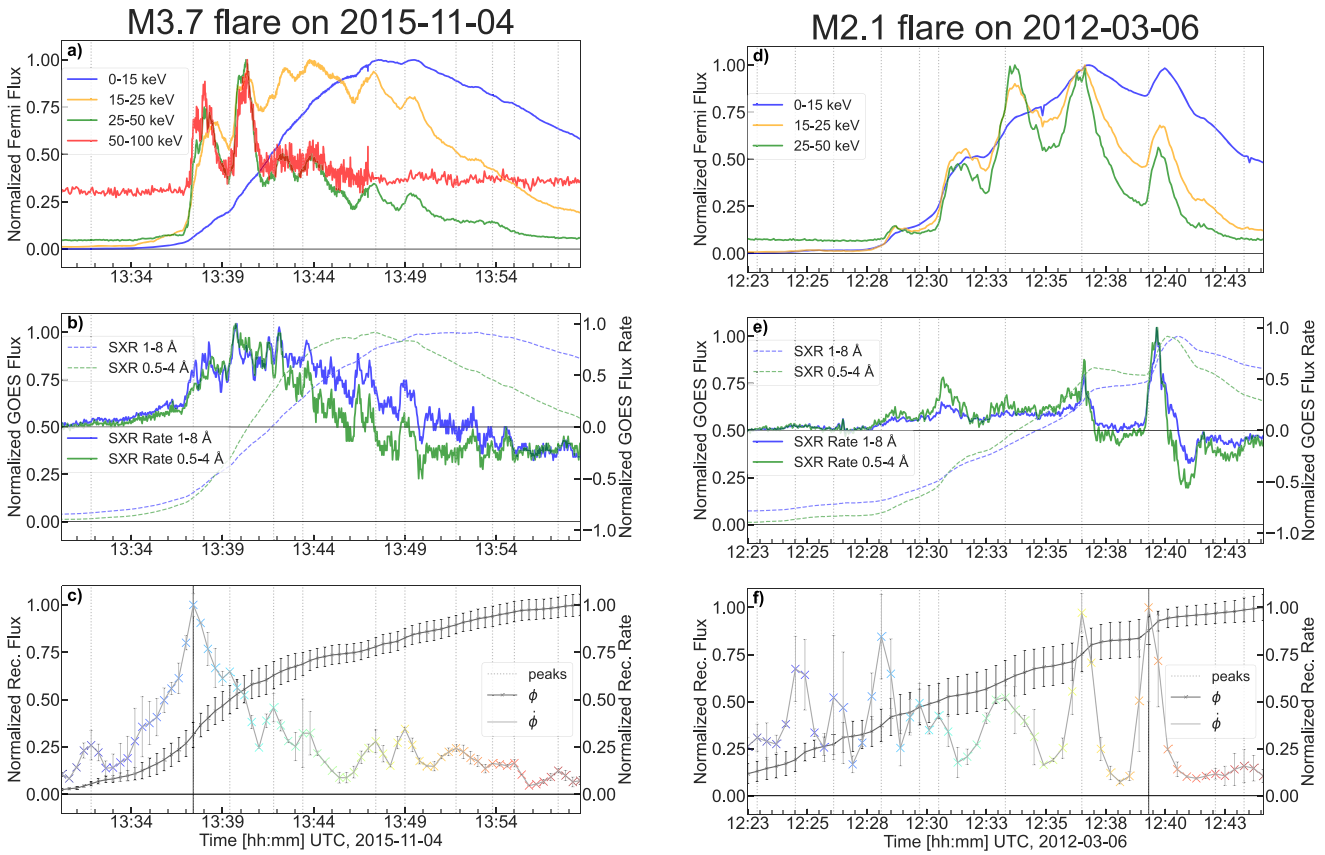

Figure 4. Comparison of fluctuations in magnetic reconnection rate with X-ray fluxes from Fermi GBM and GOES XRS during two M-class flares. The Left panel shows the M3.7 flare (see also Figure 3). The right panel shows the M2.1 flare observed on 2012 March 6. (a) Fermi GBM flux observed in four energy bands: 8–15 kev (blue), 15–25 keV (orange), 25–50 keV (green), and 50–100 keV (red). (b) Solid black and dotted gray lines show the GOES SXR fluxes; blue and green lines show GOES SXR fluxes time derivatives for 1–8 Å and 0.5–4 Å bands, respectively. (c) Reconnection flux (black) and its rate (colored to scale with temporal evolution). All of the variables have been normalized by their respective maximum. The vertical black lines mark peaks in the magnetic reconnection rate. See Section 3.1.3 for more details.

Both flares in Figure 4 serve as an illustrative example of the delay that we find between the temporal profiles of the X-ray emission and its rate and the magnetic reconnection rate. The cross correlation between the fluctuating components of the magnetic reconnection rates and the X-ray emission yields delays within 2 minutes. Here the positive delays mean that the reconnection-rate QPP happens before the X-ray QPPs, and the negative is vice versa. Interestingly, the lower amplitude bursts in the reconnection rates are not always accompanied by a corresponding burst in the HXR emission. This is especially noticeable when comparing the early phases of the Fermi GBM with the reconnection-rate profiles for the 2012 March 6 flare, shown in Figures 4((d)–(f)). For this flare, the first Fermi GBM X-ray bursts are observed only 7 minutes after the flare onset, and more than 5 minutes after the initial reconnection-rate burst ($t \approx 12{:}24{:}00$ UTC). Additionally, during the late phase ($t > 13{:}50{:}00$ UTC) of the 2015 November 4 flare, shown in Figures 4((a)–(c)), the high-energy Fermi channels (>25 keV) do not exhibit the same busts as those in the reconnection rate. In Figure 10 of the Appendix we show an additional 10 examples comparing Fermi HXR and GOES SXR QPPs with the reconnection-rate oscillations. These additional 10 examples illustrate that QPPs observed in both X-ray and the reconnection rate are not unique to the two case studies shown here, potentially being a consequence of the same process in the current sheet.

Lastly, in Figure 5 we apply the wavelet transform to characterize the QPPs in the 2015 November 4 flare using emission in the 25–50 keV, emission rate in the 1–8 Å, and the magnetic reconnection rate. The background-removed HXR and the SXR rate QPPs have very similar periods of approximately 1.8 minutes, while the reconnection rate has a higher period of 2.5 minutes. The periods in the reconnection-rate and X-ray QPPs are not the same, which is expected due to the discrepancies in the time series. Nonetheless, the wavelet power spectrum for these observations shows that similar oscillatory modes are excited cotemporally in all of the time series. We compare these results with the Fourier power spectrum and find inconsistency in the periods with the local maxima between the different observations and the wavelet results. These periods also do not match the observed oscillation periods. The Fourier power spectrum is excluded from the rest of the study since it fails to accurately represent the power of nonstationary oscillations. Furthermore, the Fourier power spectrum distribution of local maxima makes it much harder to identify QPPs that match oscillations identified in the time series data.

The cotemporal bursty signatures in both of the HXR emission observed by Fermi GBM, GOES XRS SXR emission, and the reconnection rates from SDO suggest a link between

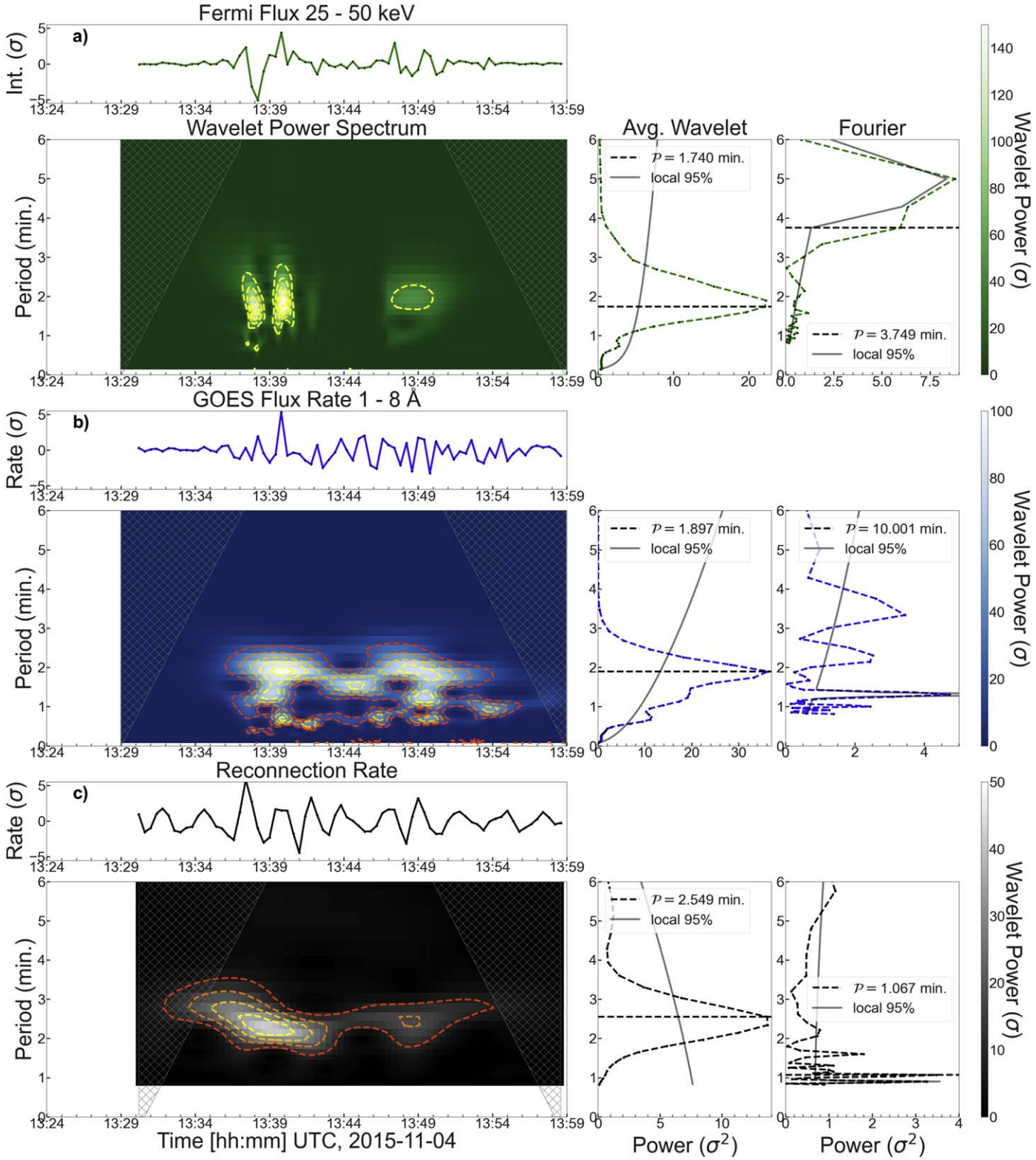

Figure 5. Wavelet and Fourier power spectra for X-ray fluxes and reconnection rate for the M3.7 2015 November 4 flare (see also Figures 3 and 4(a)–(c)). Panel (a): the detrended fluctuations in the Fermi 25–50 keV emission are shown on the top panel, its wavelet transform below it, and average wavelet power and Fourier power on the right. Panel (b): fluctuation in the GOES $1-8$ Å emission rate following the same layout as in (a). Panel (c): fluctuations in the magnetic reconnection rate with the same layout as in (a) and (b). The red-to-yellow contours on the wavelet transform maps correspond to areas where wavelet power exceeds the 95% colored noise level. See Section 3.1.3 for more details.

the two types of observations. This link is further demonstrated by the results of the wavelet transform: the cotemporal excitation of similar oscillatory modes ($\mathcal{P} \leqslant 3$ minutes) and finding QPPs in the time-averaged wavelet spectrum with similar periods (1.8 and 2.5 minutes). In Section 4 we discuss this relationship in more detail.

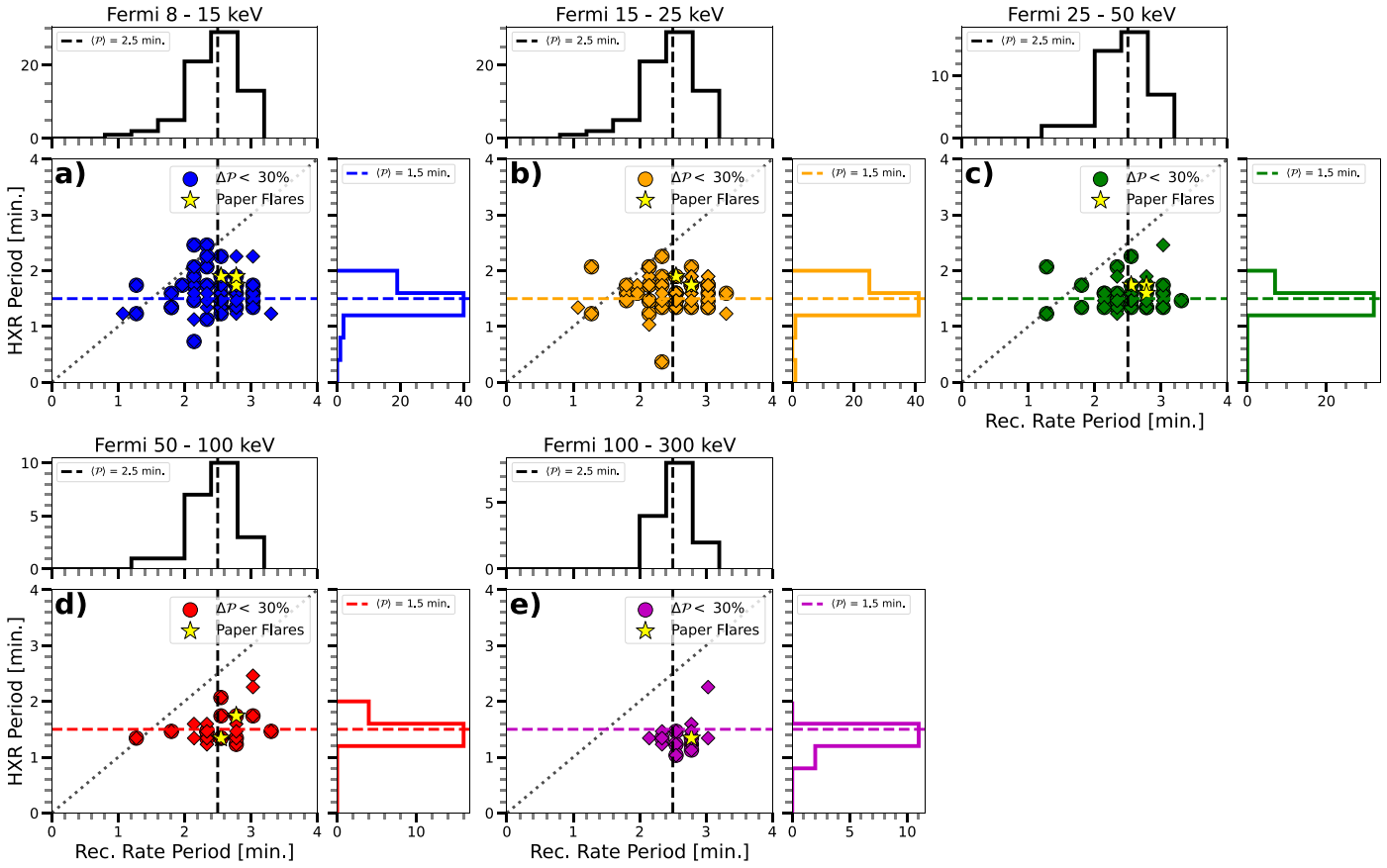

Figure 6. Periods of QPPs in HXR emission (from Fermi GBM) vs. periods of QPPs in unsigned magnetic reconnection rates for 73 flares. Panels (a)–(e) correspond to the following X-ray energy bands: (a) 8–15 keV, (b) 15–25 keV, (c) 25–50 keV, (d) 50–100 keV, and (e) 100–300 keV. QPP periods have been identified using wavelet transform. The large circles represent the flares with periods that match up to 30% between the original time series, and the background subtracted time series. The yellow stars show case studies from Section 3.1. See Section 3.2.1 for more details.

3.2. Statistical Properties of QPPs in Reconnection Rates and HXR Emission for 73 Flares

To further understand and characterize the relationships that we found for the example events in Section 3.1, we expand our analysis to 73 flares: 39 C-class, 24 M-class, and 10 X-class flares from the `RibbonDB` database.

3.2.1. Comparison of QPP Periods: Reconnection Rates and X-Ray Emission

We apply the wavelet transform to the unsigned reconnection rates of all 73 flares to find their periods. We then compare the QPP periods from the unsigned reconnection rates with those derived from the Fermi GBM HXR channels (Figure 6). First, the number of QPP observations in each energy channel varies—lower-energy channels (8–50 keV) have more events than higher-energy channels (panels (a) and (e)). Second, there is no simple mathematical relationship between the observed QPPs in the reconnection rate and the HXR Fermi observations. Rather, the periods converge in the range of 0–3 minutes. The histograms of the QPPs show that the HXR distribution peaks at around 1.5 minutes in each channel, while the reconnection-rate distribution peaks at 2.5 minutes. Therefore, on average the QPPs in the reconnection rate have larger periods than those in the HXR emission. This is the same behavior observed in the example flares (yellow stars in Figure 6) shown in Section 3.1.

In Figure 7 we compare the QPP periods from the unsigned reconnection rate and GOES XRS flux derivative. We find the same number of events in both the GOES long and short wavelength bands, since they are much closer in energy range than the Fermi GBM channels. Similar to Figure 6, the QPPs in GOES XRS flux derivative have no polynomial relationship with QPSs in reconnection rate. Instead we find the same convergence in periods below 3 minutes. Coincidentally, the SXR rate QPPs also have a peak in their distribution at approximately 1.5 minutes. Therefore, as was the case in the Fermi HXR observation, the SXR emission rate QPPs have a shorter period on average than the reconnection rates.

Our results suggest that the wavelet transform is capable of characterizing the QPPs in the X-ray and reconnection-rate data. This is confirmed by the overall agreement between QPPs observed in the isolated fluctuating component of each time series, and the time series containing background trends. On average the HXR emission and SXR emission rates have the same QPP periods of 1.5 minutes, which is lower than the 2.5 minute QPP periods in the reconnection rates. This statistical relationship suggests that the HXR and SXR QPPs are intrinsically linked to the same driving mechanics related to the reconnection-rate QPPs.

3.2.2. Delay in X-Ray Emission

When examining the individual examples presented in Figure 4, we found that both the Fermi GBM and GOES

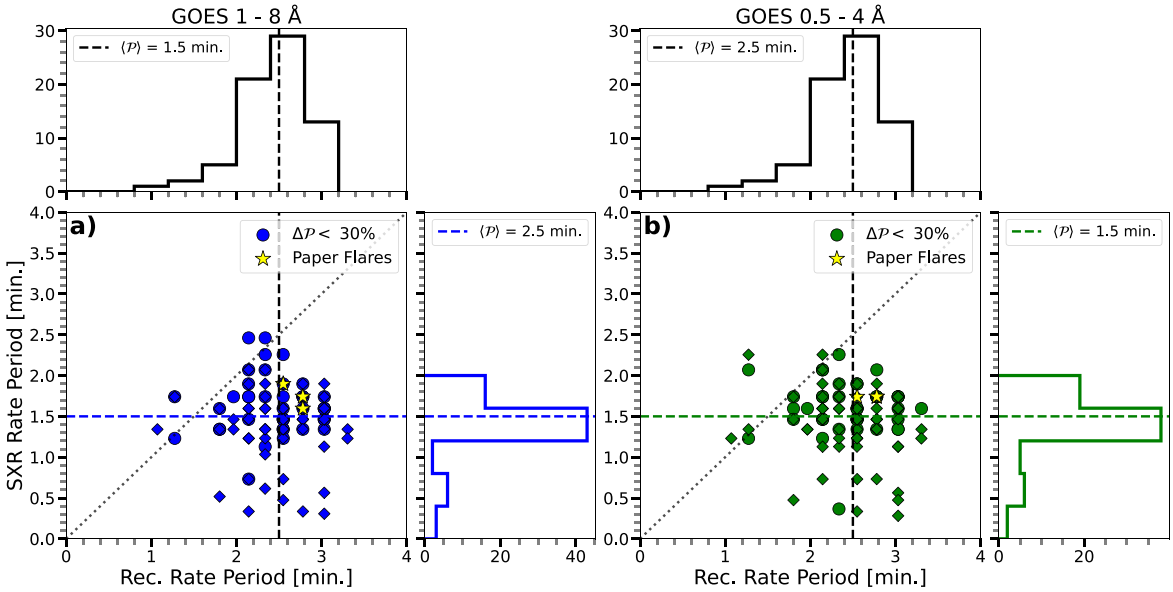

Figure 7. Periods of QPPs in SXR emission rates vs. periods of QPPs in unsigned magnetic reconnection rates for 73 flares: (a) 1–8 Å and (b) 0.5–4 Å passbands. The large circles represent the flares with periods that match up to 30% between the original time series, and the background subtracted time series. The yellow stars show case studies from Section 3.1. See Section 3.2.1 for more details.

XRS rate oscillations are delayed from the reconnection-rate bursts. To evaluate the delay time for each flare, we examine the cross correlation between the background subtracted reconnection rate and the X-ray data. The location of the cross-correlation maxima determines the delay time between the oscillations. We determine delay calculations relative to the reconnection rate, therefore positive values imply that the reconnection-rate oscillation precedes the X-ray oscillations, while a negative value is the opposite.

In Figure 8 we show the delay time of Fermi GBM HXR emission in each channel. Each energy channel shows very similar behavior, highlighting that both the low and high HXR QPPs are connected to the same dynamical process. We see a distribution of delay times ranging from ±300 s. The lower energy channels (8–50 keV) show a peak in the distribution of delays at 24 s. This maxima is not present in the higher-energy channels (50–300 keV). Instead, we get somewhat of a more uniform distribution of delays. This can be attributed to the low number of events that have clean HXR oscillations in these channels (23 and 14 flares, respectively). Therefore, the HXR oscillations sometimes precede the reconnection-rate bursts, but mostly occur after the reconnection-rate oscillation by a couple of seconds to minutes. On average, the HXR oscillations occur 24 s after the onset of the reconnection-rate QPPs.

Figure 9 presents the cross-correlation time delay time between the GOES XRS emission rate QPPs (HXR emission proxy) and the reconnection-rate oscillations. The distributions of delays for both channels (1–8 Å and 0.5–4 Å) are spread from −60 to 300 s. Furthermore, these distributions peak at 24 s, suggesting, as was the case for the HXR (Figure 8), that the SXR rate oscillations occur after the reconnection rate. Specifically we find that, on average, the reconnection-rate burst onset precedes the SXR rate QPPs by 24 s. Thus, the GOES SXR emission rate QPPs have the same average statistical characteristics found for the Fermi HXR QPPs. This is further evidence that although the SXR and HXR emission have different sources (flare footpoints and loop tops, and flare loops, respectively), their QPPs suggest a connection to the same oscillatory particle acceleration episodes.

Since most of the X-ray observations show a peak in their distribution at 24 s we further examine if the result is a real phenomenon or an artifact in the data. A delay time of 24 s corresponds to the time cadence of the AIA observations used to calculate the reconnection flux and rates. Therefore, the 24 s delay could be an error introduced by the finite difference scheme used to calculate the reconnection rate. We verify if the numerical scheme introduced the delay between the HXR and reconnection-rate QPPs by changing the numerical differential scheme from the central difference scheme, which is the default of the *NumPy* library (Harris et al. 2020), to finite forward and backward schemes. We find that changes in the numerical approximation of the derivatives cause no significant changes to the location of the peak of the distributions when using forward differentiation. When using the backward differentiation scheme, the peaks in the delay distributions shift to 5 s. Therefore, the order in which QPP precedes (reconnection rate) remains unchanged when varying the differentiation scheme. Yet the average value 24 s delay time should be interpreted as an upper limit because of the value's sensitivity to changes in differentiation schemes.

Table 1 summarizes the results of this section. The oscillation periods presented in our statistical analysis range from tens of seconds to 4 minutes. On average, the reconnection-rate oscillations have a period of 2.5 minutes, which is larger than the X-ray average QPP of 1.5 minutes. The reconnection-rate QPPs onset precedes the X-ray QPPs in the lower energy channels (>50 keV) on average by 24 s. The higher-energy X-ray channels (⩾50 keV) QPPs on average occur more synchronously to the reconnection-rate QPPs. We note, however, that this result is subject to statistical biases due to the low number of flares (23 and 14, respectively) that exhibit clear QPPs in the higher-energy channels.

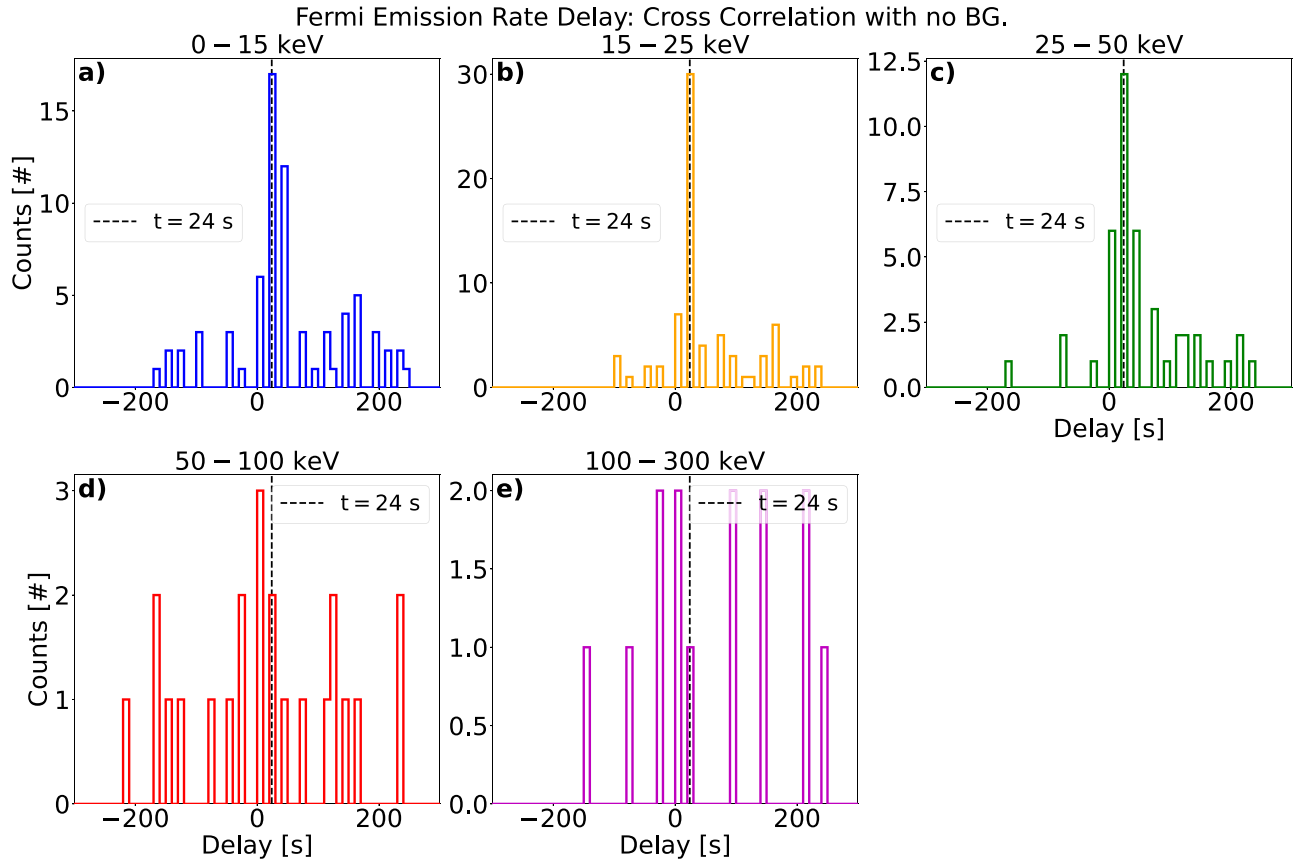

Figure 8. Distributions of delay times between HXR emission and magnetic reconnection rate for 73 flares. Panels (a)–(e) correspond to HXR emission in (a) 8–15 keV, (b) 15–25 keV, (c) 25–50 keV, (d) 50–100 keV, and (e) 100–300 keV energy bands. Dashed vertical lines show 24 s of delay time from cotemporal emission. Positive and negative delays are defined as reconnection-rate QPP preceding and following the X-ray QPP, respectively. See Section 3.2.2 for more details.

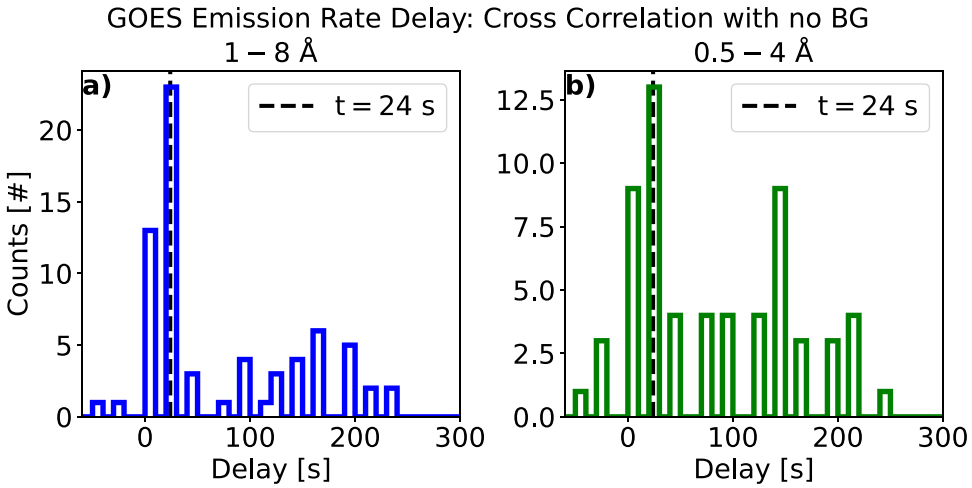

Figure 9. Histograms showing the SXR emission rate delay from the magnetic reconnection rate for 73 flares. The left and right panels show 1–8 Å and 0.5–4 Å channels, respectively. See Section 3.2.2 for more details.

4. Discussion

Our spatiotemporal analysis of flare ribbons and reconnection-rate time series showed that magnetic flux swept by flare ribbons produces bursts or oscillations in magnetic reconnection rates. Bursty magnetic reconnection is associated with PI and the formation and dynamics of plasmoids of different scales within the current sheet (Shibata & Tanuma 2001). Analytical work by Wyper & Pontin (2021) suggests that these swirls and waves and swirls shown in Figures 2 and 3 could be related to the PI. In particular, Wyper & Pontin (2021) used an analytical representation of an eruptive flux rope and flaring loop system to show that plasmoid structures and their motions within the current sheet were connected to the fine structure and their apparent motion displayed in the flare ribbons.

Brannon et al. (2015) analyzed the M7.3 class flare on 2014 April 18 finding QPP signatures in the position and Doppler shifts of sawtooth fine-structure (wave breaks) patterns. These oscillations were found to have periods of 140 s and 100 to

Table 1
Summary of the Statistical Analysis of QPP Periods and Delay Times in HXR Emission for 73 Analyzed Flares

Observation	Number of Observed Flares	Mean $\mathcal{P}(\dot{\Phi})$ (min.)	Mean Delay (sec.)
Rec. Rates	73	2.5	N/A
Fermi 8–15 keV	72	1.5	24
Fermi 15–25 keV	73	1.5	24
Fermi 25–50 keV	43	1.5	24
Fermi 50–100 keV	23	1.5	20
Fermi 100–300 keV	14	1.5	16
GOES 1–8 Å	73	1.5	24
GOES 0.5–4 Å	73	1.5	24

200 s, respectively. Coincidentally, these are within the period range of detected QPPs from the reconnection rates in our sample of 73 flares (24–240 s). Specifically, we found that the M7.3 on the 2014 April 18 flare had a reconnection-rate QPP of 140 s, which agrees with the authors' findings. Brannon et al. (2015) suggested that a possible explanation of the oscillations found in the motions of the fine structure in the flare ribbon was the PI in the above loop-top region of the flare system. While Parker & Longcope (2017) proposed the flare ribbon fine structure forms as the TI develops and drifts due to shear flow along the legs of a flare loop rather than in the flare current sheet.

Using IRIS SJIs in the 1330 and 1400 Å filters we found fine structure in the flare ribbon fronts evolving throughout the flares. We found that the bursty quasiperiodic evolution of the reconnection rate occurred cotemporally with the development and evolution of fine structure in the flare ribbon fronts. This behavior is presented in Figures 2 and 3. Yet, for now we did not isolate the contributions of the flare ribbon fine structure from the cumulative evolution of the flare ribbon. This step will be necessary to explore the contribution of the fine structure to the reconnection-rate bursts. A future study will be conducted to explore this relationship, and uncover current sheet dynamics that contribute to the formation and evolution of the flare ribbon fine structure. Furthermore, in this study we used the AIA 1600 Å observations to derive the reconnection flux and rate. The lower spatial resolution and saturation issues of this passband complicated the identification of the location of the fine-structure development in our observations. Thus, to explore the relationship between the fine-structure evolution and the reconnection-rate burst, we will need a data set with very high spatial and temporal resolution. To summarize, we find that the larger-scale cumulative flare ribbon evolution, which contains the regions in which the fine structure develops, results in a bursty profile of the reconnection rate, as shown in Figure 1.

We discard the possibility that bursts in the reconnection rate are a consequence of a systemic bias in our masking algorithm, since we find reconnection-rate QPPs in both positive- and negative-polarity ribbons independently. For example, Figure 1 shows that although the morphology of the flare ribbon is very different, the reconnection flux/rate approximately balance each other in the opposite polarities through the flare. Additionally, Figure 10 shows 10 examples of the reconnection flux and rates for the positive and negative-polarity ribbons. As mentioned before, the reconnection flux and rates approximately balance each other. Furthermore, almost simultaneous signatures of bursts in the HXR emission suggest that the reconnection-rate bursts are a real physical phenomenon that could be linked with these HXR bursts and current sheet dynamics.

Naus et al. (2022) used high-resolution IRIS observations to compare the evolution of ribbon fronts with HXR emission from Fermi GBM and the Reuven Ramaty High Energy Solar Spectroscopic Imager (RHESSI; Lin et al. 2002). They found that the ribbon front exhibits highly structured and dynamic changes in their local widths. These intermittent changes in widths are consistent with our observations of the ribbon sweeping new reconnected flux and producing bursty reconnection rates. Additionally, they found that the evolution of ribbon front widths was cospatial and cotemporal with the bursty UV and HXR emission during the late phase of bursty reconnection of the flare. This suggests that in the early evolution of the flare, bursty reconnection does not guarantee nonthermal particle acceleration. Here we find similar decoupling between the reconnection-rate and HXR emission in the early phase of the flare (see Section 3.1.3).

Numerical simulations and observations have allowed the exploration of how HXR emission is suppressed by the change in the magnetic field shear of the flare loops. Qiu & Cheng (2022) found that the lag in HXR emission to the UV emission from flare ribbons corresponds to the strong to weak magnetic field shear evolution of the flare loops (inferred from flare ribbons), consistent with the 3D MHD simulation by Dahlin et al. (2022). They presented a clear connection between the shear inferred from the flare loops and ribbons and the variation of the guide field (magnetic field component perpendicular to the reconnection plane) in the reconnection sheet, where these values cannot be measured. Other numerical experiments by Arnold et al. (2021) show that the presence of a strong guide field suppresses the particle acceleration efficiency of plasmoids.

Figure 4 compares the temporal evolution of the reconnection rates with the HXR emission from Fermi GBM and GOES XRS emission rates (a proxy for HXRs). We found that bursts in the reconnection rates (shown with gray vertical lines in Figure 4) are associated with nearly cotemporal HXR emission. These results suggest that there might be some current sheet dynamics that link these two processes. Similarly, Clarke et al. (2021) found cotemporal QPPs during the 2015 November 4 M3.7 flare in multiple wavelengths: 2.5 MHz, 171 Å, 1600 Å, 1–8 Å, and 25–50 keV. The 2 minute periodicity found in the EUV, SXR, and HXR implies a common progenitor for the QPPs. Additionally, they find that the EUV and X-ray pulsations are located in the source of HXR flare loop footpoints. Therefore, intermittently accelerated electrons during the reconnection process form bursty emission in the EUV and X-ray. A possible explanation for this intermittent acceleration of the electrons is intermittent magnetic reconnection modulated by the PI. Our results provide additional evidence of this intermittent magnetic reconnection. We observe 2.5 minute reconnection-rate QPPs during this M3.7 flare, which provides additional evidence that oscillatory reconnection, perhaps modulated by the PI, drives the bursty emission in the HXR and SXR rates.

In the PI-driven magnetic reconnection scenario, the current sheet would be filled with plasmoids that can interact and merge accelerating populations of particles that can later produce the HXR and SXR emission (Drake et al. 2006;

Guidoni et al. 2016, 2022). Single magnetic island accelerators have been found to provide insufficient energy gains to reproduce HXR emission (Drake et al. 2006; Guidoni et al. 2016). Yet, Guidoni et al. (2022) analytically showed that the transport of electrons between consecutive magnetic islands with similar accelerator efficiencies leads to the nonthermal electron distribution with sufficient energy to produce HXR emission due to electron collisions in the chromosphere. Thus, the ejected plasmoid populations can merge with one another to form larger plasmoids (Loureiro et al. 2007; Uzdensky et al. 2010), all while accelerating particles due to magnetic mirroring within them. These large plasmoids can then reconnect with the flare loops and transfer high-energy particle populations to them, which could later propagate to the chromosphere. Once in the denser chromospheric layers, the HXR and SXR emissions can form as described in the standard flare model.

Additionally, we have found that bursts in the reconnection rates behave like QPPs, and estimated the periods for 73 flares using the Wavelet transform. We found reconnection-rate oscillation to have periods ranging from almost 1 minute to 4 minutes, with an average period of 2.5 minutes. These oscillations appear to be related to the QPPs detections in the Fermi GBM and GOES XRS observations, even when the X-ray QPPs shown in Figures 6 and 7 have shorter periods, on average of 1.5 minutes. We suggest that the subminute discrepancies are related to the lower cadence in the AIA observations (24 s) used to calculate the reconnection flux and rates. Features in the reconnection-rate time series with a timescale lower than 24 s are temporally averaged out in each read by the AIA instrument. As a consequence, the time and amplitude of each of the reconnection-rate bursts (local maxima in the time series) have an uncertainty. In addition, the reconnection-rate wavelet transform excludes many possible subminute oscillations due to the 48 s Nyquist limit. Both of these consequences of the lower cadence of AIA data can lead to errors in our estimate of the reconnection-rate oscillation periods. Another possibility is that the particle acceleration evident as X-ray QPP is caused by different current sheet dynamics, leading to the differences between the reconnection-rate oscillations and the X-ray QPPs.

Other mechanisms to explain QPPs in the reconnection rate include recent findings by Thurgood et al. (2017) where magnetic reconnection in a 3D null point can occur periodically and excite MHD waves. A 2D simulation showed that oscillating plasmoids produced by the subsequent merging of two initial plasmoids can excite oscillations of the current sheet loop tops as they reconnect (Jelínek et al. 2017). Takahashi et al. (2017) used a 2D simulation of reconnection in a current sheet below an eruptive CME and found that for large values of the Lundquist number $S = 5.6 \times 10^3$ and 2.8×10^4 (PI unstable), periodic reconnection would produce reconnection jets that excite oscillations at the top and bottom of the current sheet. These jets then could form shocks that are capable of accelerating particles with similar QPP periods of the reconnection-rate oscillations. We can summarize these mechanisms as MHD wave-driven magnetic reconnection. The coupling of these waves with the termination shock above the flare loop can accelerate the coronal particles to produce the observed X-ray QPPs.

Our study does not address the specific contribution of each mechanism in the production of the QPPs in the reconnection rates and the HXR emission and how the QPPs differ slightly in their periods. The spatiotemporal analysis of the flare ribbons suggests that the current sheet undergoes PI and that plasmoids and their dynamics should be related to the generation of the QPPs and bursty signatures presented in this work. Still, we are unable to determine whether the HXR emission is driven by termination shocks produced by the reconnection jets or the merging of plasmoids populated with accelerated electrons. There is a probability that both mechanisms are present during magnetic reconnection in large flares. In the future, it will be of much interest to evaluate the relative contributions of each mechanism to the production of QPPs in the X-ray.

Finally, we find that the delay time between the reconnection-rate oscillations and the X-ray QPPs is within the range of seconds to minutes. On average, both the Fermi GBM and GOES XRS QPPs are delayed by 24 s. We verify that the delay, which matches the AIA temporal cadence, is not a consequence of the numerical differentiation scheme. Specifically, we found that the statistical properties of the delay distribution are independent of the finite difference scheme when using forward or central differentiation to calculate the reconnection rates. When using backward differentiation, the average delay between the QPPs decreases to 5 s. Yet, the overall relationship of the reconnection-rate oscillation onset occurring a few seconds to minutes before the X-ray QPPs remains the same. Therefore, the delay is either a consequence of the differences in cadences between the instruments or a physical mechanism causing the delay. Miklenic et al. (2007) and Veronig & Polanec (2015) found similar results when comparing reconnection rates with the HXR emission observed by RHESSI and GOES SXR emission rate. They interpret the newly brightened H_α/EUV/UV flaring kernels, which are used to track the reconnection flux evolution and HXR emission to be produced by two types of nonthermal electrons. The first type would correspond to a smaller population of nonthermal electrons accelerated within the reconnection site that produces the bright H_α/EUV/UV kernels. The second larger population of nonthermal particles would be accelerated at a different location, possibly at the flare loop tops, providing a delay in the emission burst relative to the reconnection-rate burst. To our knowledge, there is no observational study nor simulation that provides evidence of this delay between flare kernels brightening and the HXR emission and their association with these different nonthermal electron populations. Exploring the reason (s) for this delay will be the focus of a future study.

We hope that multiple-viewpoint observations will help determine which mechanism is driving the QPPs in the X-rays and reconnection rates. For example, Hayes et al. (2019) presented on-limb evidence of EUV and SXR QPPs during the X8.2 flare on 2017 September 10, with periods of approximately 65 and 150 s during the impulsive and decay phases. A key result from their study was that using AIA 131 Å, they found downward plasma motions along the current sheet that impact the top of the flaring loop arcade. These downward motions are cotemporal with the decay phase QPPs, suggesting a link between these downward motions in the current sheet and the QPP signals. These structures could be large-scale plasmoids exiting the current sheet and merging with the flare loop tops. Therefore, cotemporal observation of the on-disk observations of the flare ribbon and off-limb observation of the loop structures during the flare could allow a more complete understanding of the full mechanisms at play for the generation

of the QPPs in the HXR emission and reconnection rates. Coordinated observations between SDO (or other ground-based/geosynchronous instrument) and Solar Orbiter (Müller et al. 2013, 2020) will provide opportunities for these types of studies when the two spacecraft have a separation angle of $\approx 90^{\circ}$.

5. Conclusions

In this study we have analyzed oscillations in the magnetic reconnection rate and compared them with QPPs in Fermi GBM and GOES XRS observations for 73 flares from the `RibbonDB` database (Kazachenko et al. 2017). Our analysis includes the spatiotemporal comparison of flare ribbons observed with AIA 1600 Å and IRIS SJI 1330 Å and 1400 Å (when available), time series of the reconnection fluxes/rates, HXR emission ranging from 0 to 300 keV, and SXR emission/rates in the 1–8 Å and 0.5–4 Å. Our findings are summarized below:

1. For the first time, we find that magnetic reconnection, as described by reconnection rates derived from flare ribbons, occurs in bursts. These bursts on average account for 75% of the total reconnection flux of each of the 73 flares in our sample. The periods are on the order of minutes ranging from 1 to 4 minutes, with an average of 1.5 minutes.
2. From the high-resolution IRIS SJI observations of eight C- to X-class flares, we find that the fine structure in the flare ribbons is associated with periodic modulations in the ribbon fronts (Naus et al. 2022), wave-break patterns, and swirls (Brannon et al. 2015; Parker & Longcope 2017). These fine-structure patterns have been previously associated with the PI and the existence of plasmoid structures in the current sheet above the flaring loops.
3. We find X-ray QPPs that are delayed by up to a minute from bursts in the reconnection rates. The delay time of the Fermi and GOES observations is 24 s on average, suggesting that the particle acceleration of nonthermal particles that interact with the chromosphere and produce the flaring ribbon kernels and the emission of SXR and HXR might happen at different locations within the current sheet.
4. We suggest that nearly cotemporal QPP bursts in the reconnection rates and HXR emission provide evidence of oscillatory process in the reconnection region and plasmoid dynamics (Kliem et al. 2000; Lynch et al. 2016; Takahashi et al. 2017). This in turn leads to bursty particle acceleration via plasmoid dynamics or wave particle interactions (Drake et al. 2006; Guidoni et al. 2016; Takahashi et al. 2017). Our observational estimates could be used for comparison with models of bursty or oscillatory reconnection.

Acknowledgments

We acknowledge support from NASA LWS 80NSSC19K0910, 80NSSC19K0070, NASA ECIP NNH18ZDA001N, and NSF CAREER SPVKK1RC2MZ3 (MDK, MFCA). Support for this work is provided by the National Science Foundation through the DKIST Ambassadors program, administered by the National Solar Observatory and the Association of Universities for Research in Astronomy, Inc. B.J.L. acknowledges support from NASA LWS 80NSSC21K1325, NASA XRP 80NSSC22K0674, and NSF AGS 2147399. M.F.C.A. would also like to thank Dr. Ryan French for the valuable discussions on the implementation of wavelet transform analysis to detect QPPs.

Appendix
Supplemental Figures

Figure 10 shows 10 example flares from the 73 included in the study that exhibit clear reconnection-rate oscillation on each polarity flare ribbon. Each panel shows the reconnection flux and rates derived from flare ribbons from each polarity of the active region. Table 2 includes the date and start time, GOES class, NOAA active region number and oscillation period of each of the 73 flares included in our study.

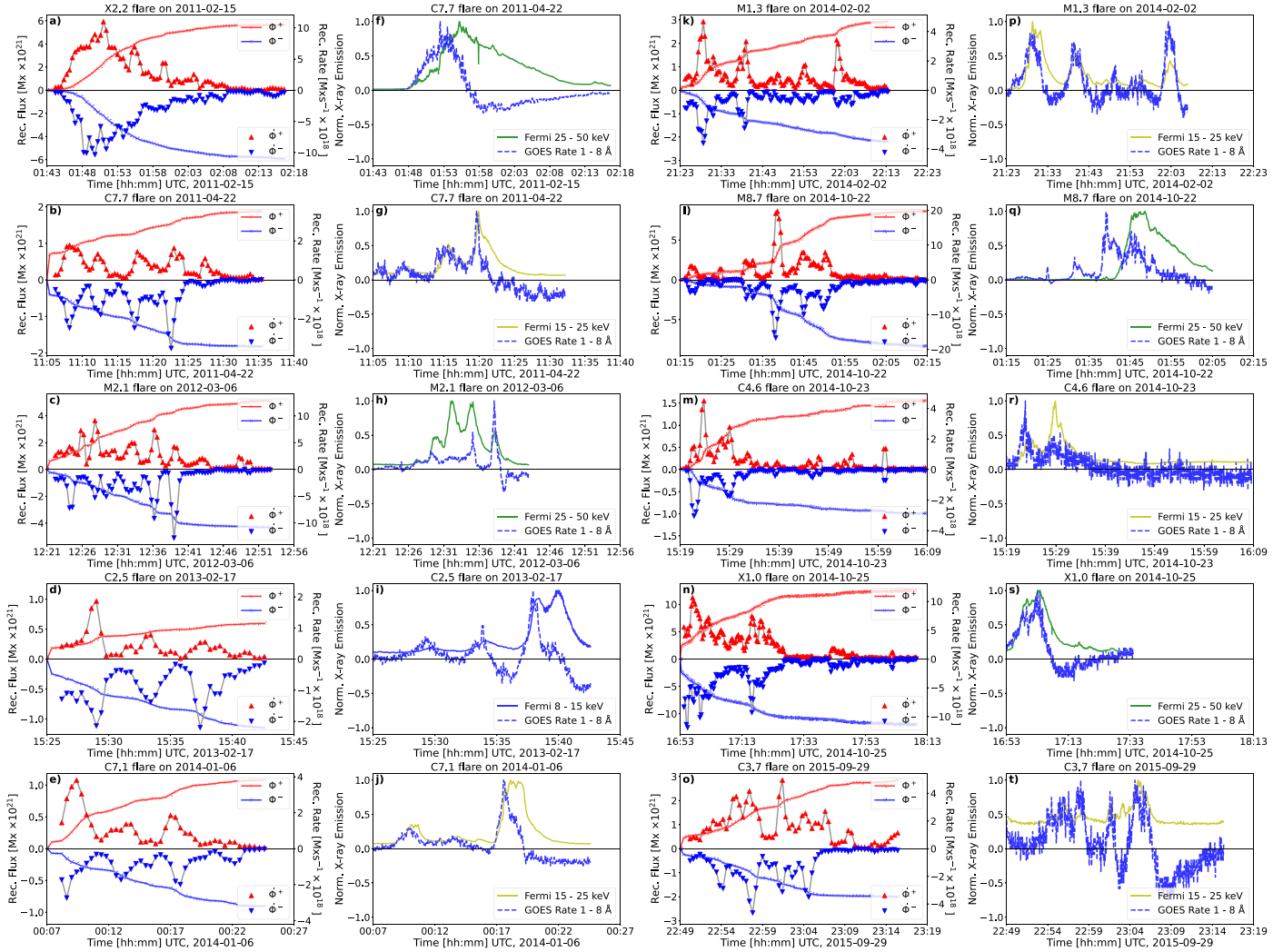

Figure 10. Ten example flares with oscillations (QPPs) in the reconnection rates and X-ray lightcurves. Panels (a)–(e) and (k)–(o) show reconnection fluxes (crosses) and reconnection flux rates (triangles) where red and blue colors correspond to positive and negative polarities, respectively. Panels (f)–(j) and (p)–(t) show Fermi HXR and GOES SXR rate lightcurves.

Table 2
Magnetic Reconnection-rate Oscillation Period for the 73 Flares Included in Our Study

Date	Flare Start Time (UTC)	GOES Flare Class	NOAA AR	$\mathcal{P}(\dot{\Phi})$ (min.)
2010-06-12	00:30	M2.0	11081	1.80
2010-11-11	15:54	C4.3	11123	2.14
2010-11-15	07:28	C2.3	11124	4.29
2011-02-13	17:28	M6.6	11158	4.29
2011-02-15	01:44	X2.2	11158	3.93
2011-03-09	23:13	X1.5	11166	2.78
2011-03-10	03:50	C2.9	11166	2.78
2011-03-25	23:08	M1.0	11176	1.27
2011-04-22	04:35	M1.8	11195	3.31
2011-04-22	11:07	C7.7	11195	4.68
2011-09-06	22:12	X2.1	11283	0.83
2011-09-07	22:32	X1.8	11283	2.14
2011-10-15	13:56	C5.0	11319	2.78
2011-11-06	14:30	C5.3	11339	5.56
2011-11-07	03:05	C3.5	11339	2.55
2011-12-26	20:12	M2.3	11387	2.34
2012-01-14	03:19	C2.1	11396	4.29
2012-03-06	12:23	M2.1	11429	3.03

Table 2
(Continued)

Date	Flare Start Time (UTC)	GOES Flare Class	NOAA AR	$\mathcal{P}(\dot{\Phi})$ (min.)
2012-03-19	21:55	C3.5	11434	0.83
2012-03-25	00:15	C3.0	11444	1.97
2012-05-11	09:37	C2.3	11476	3.03
2012-05-13	07:21	C7.0	11476	6.61
2012-06-05	20:49	C4.2	11499	1.28
2012-07-02	14:32	C1.7	11513	3.93
2012-07-02	19:34	C2.5	11515	2.34
2012-07-04	01:30	C5.1	11515	2.34
2012-07-04	04:28	M2.3	11515	1.97
2012-07-04	09:47	M5.3	11515	3.03
2012-07-05	20:09	M1.6	11515	3.03
2012-07-10	12:08	C5.5	11520	2.34
2012-10-24	09:06	C2.9	11598	3.30
2013-02-17	15:26	C2.5	11675	2.14
2013-04-11	06:55	M6.5	11719	2.34
2013-08-31	17:20	C2.6	11836	4.68
2013-10-11	22:56	C6.3	11861	0.83
2013-10-13	00:12	M1.7	11865	1.39
2013-10-14	12:56	C8.0	11865	2.14
2013-10-22	04:12	C4.0	11875	1.65
2013-10-28	11:32	M1.4	11877	2.34
2013-11-07	14:15	M2.4	11890	0.83
2013-11-10	05:08	X1.1	11890	2.55
2013-12-14	11:00	C2.3	11917	1.52
2014-01-06	00:08	C7.1	11944	4.29
2014-01-07	04:40	C2.4	11944	1.39
2014-02-02	21:24	M1.3	11967	5.10
2014-02-13	12:33	C3.0	11974	1.80
2014-02-14	02:40	M2.3	11974	3.03
2014-04-23	00:48	C4.3	12038	1.97
2014-05-03	05:31	C5.3	12051	3.03
2014-06-18	03:12	C4.0	12087	7.86
2014-07-30	16:00	C9.0	12127	2.14
2014-09-10	17:21	X1.6	12158	3.93
2014-10-20	16:00	M4.5	12192	4.29
2014-10-22	01:16	M8.7	12192	6.06
2014-10-22	14:02	X1.6	12192	0.83
2014-10-23	15:20	C4.6	12192	5.56
2014-10-25	16:55	X1.0	12192	3.60
2014-10-26	10:04	X2.0	12192	5.56
2014-12-09	09:58	C8.6	12230	3.03
2014-12-17	21:02	C7.1	12242	1.80
2014-12-19	09:31	M1.3	12242	2.55
2014-12-20	00:11	X1.8	12242	2.34
2015-01-06	05:16	C6.0	12253	1.80
2015-03-12	11:38	M1.6	12297	3.31
2015-03-15	11:31	C6.8	12297	1.80
2015-04-18	18:09	C2.9	12321	1.27
2015-06-22	17:39	M6.5	12371	5.10
2015-08-21	09:34	M1.4	12403	1.52
2015-08-22	09:09	C5.1	12403	2.34
2015-09-27	10:20	M1.9	12422	1.80
2015-09-28	07:27	M1.1	12422	1.39
2015-09-29	22:50	C3.7	12422	1.80
2015-11-04	13:31	M3.7	12443	2.55

ORCID iDs

Marcel F. Corchado Albelo https://orcid.org/0000-0003-1597-0184
Maria D. Kazachenko https://orcid.org/0000-0001-8975-7605
Benjamin J. Lynch https://orcid.org/0000-0001-6886-855X

References

Arnold, H., Drake, J., Swisdak, M., et al. 2021, PhRvL, 126, 135101
Aschwanden, M. 2011, Self-Organized Criticality in Astrophysics (Berlin: Springer)
Atwood, W. B., Abdo, A. A., Ackermann, M., et al. 2009, ApJ, 697, 1071
Auchère, F., Froment, C., Bocchialini, K., Buchlin, E., & Solomon, J. 2016, ApJ, 825, 110
Barnes, W. T., Bobra, M. G., Christe, S. D., et al. 2020, ApJ, 890, 68
Bárta, M., Büchner, J., Karlický, M., & Skála, J. 2011, ApJ, 737, 24
Bárta, M., Karlický, M., & Žemlička, R. 2008, SoPh, 253, 173
Benz, A. O. 2017, LRSP, 14, 2
Bhattacharjee, A., Huang, Y.-M., Yang, H., & Rogers, B. 2009, PhPl, 16, 112102
Bobra, M. G., Xudong, S., & Turmon, M. J. 2021, mbobra/SHARPs: SHARPs 0.1.0 (2021-07-23), v0.1.0, Zenodo, doi:10.5281/zenodo.5131292
Bornmann, P. L., Speich, D., Hirman, J., et al. 1996, Proc. SPIE, 2812, 291
Brannon, S. R., Longcope, D. W., & Qiu, J. 2015, ApJ, 810, 4
Broomhall, A. M., Davenport, J. R., Hayes, L. A., et al. 2019, ApJS, 244, 44
Brown, J. C. 1971, SoPh, 18, 489
Carmichael, H. 1964, in AAS-NASA Symposium, The Physics of Solar Flares, ed. W. N. Hess (Washington, DC: NASA), 451
Chamberlin, P. C., Woods, T. N., Eparvier, F. G., & Jones, A. R. 2009, Proc. SPIE, 7438, 743802
Clarke, B. P., Hayes, L. A., Gallagher, P. T., Maloney, S. A., & Carley, E. P. 2021, ApJ, 910, 123
Dahlin, J. T., Antiochos, S. K., Qiu, J., & DeVore, C. R. 2022, ApJ, 932, 94
De Pontieu, B., Polito, V., Hansteen, V., et al. 2021, SoPh, 296, 84
De Pontieu, B., Title, A. M., Lemen, J. R., et al. 2014, SoPh, 289, 2733
Drake, J. F., Swisdak, M., Che, H., & Shay, M. A. 2006, Natur, 443, 553
Fletcher, L., Dennis, B. R., Hudson, H. S., et al. 2011, SSRv, 159, 19
Forbes, T., & Lin, J. 2000, JASTP, 62, 1499
Forbes, T. G. 2000, JGRA, 105, 23153
Forbes, T. G., & Isenberg, P. A. 1991, ApJL, 373, 294
Forbes, T. G., & Priest, E. R. 1984, SoPh, 94, 315
French, R. J., Matthews, S. A., Jonathan Rae, I., & Smith, A. W. 2021, ApJ, 922, 117
Furth, H. P., Killeen, J., & Rosenbluth, M. N. 1963, PhFl, 6, 459
Graham, D. R., & Cauzzi, G. 2015, ApJL, 807, L22
Guidoni, S. E., DeVore, C. R., Karpen, J. T., & Lynch, B. J. 2016, ApJ, 820, 60
Guidoni, S. E., Karpen, J. T., & DeVore, C. R. 2022, ApJ, 925, 191
Harris, C. R., Millman, K. J., van der Walt, S. J., et al. 2020, Natur, 585, 357
Hayes, L. A., Gallagher, P. T., Dennis, B. R., et al. 2019, ApJ, 875, 33
Hirayama, T. 1974, SoPh, 34, 323
Hoeksema, J. T., Liu, Y., Hayashi, K., et al. 2014, SoPh, 289, 3483
Huang, Y.-M., & Bhattacharjee, A. 2010, PhPl, 17, 062104
Huang, Y.-M., & Bhattacharjee, A. 2016, ApJ, 818, 20
Hudson, H. S. 2011, SSRv, 158, 5
Inglis, A. R., Ireland, J., Dennis, B. R., Hayes, L., & Gallagher, P. 2016, ApJ, 833, 284
Inglis, A. R., Ireland, J., & Dominique, M. 2015, ApJ, 798, 2
Jelínek, P., Karlický, M., Van Doorsselaere, T., & Bárta, M. 2017, ApJ, 847, 98
Ji, H., Daughton, W., Jara-Almonte, J., et al. 2022, NatRP, 4, 263
Karpen, J. T., Antiochos, S. K., DeVore, C. R., & Golub, L. 1998, ApJ, 495, 491
Karpen, J. T., Antiochos, S. K., & DeVore, C. R. 2012, ApJ, 760, 81
Kazachenko, M. D., Albelo-Corchado, M. F., Tamburri, C. A., & Welsch, B. T. 2022, SoPh, 297, 59
Kazachenko, M. D., Lynch, B. J., Welsch, B. T., & Sun, X. 2017, ApJ, 845, 49
Kliem, B., Karlický, M., & Benz, A. O. 2000, A&A, 360, 715
Kopp, R., & Pneuman, G. 1976, SoPh, 50, 85
Kou, Y., Cheng, X., Wang, Y., et al. 2022, NatCo, 13, 7680
Lemen, J. R., Title, A. M., Akin, D. J., et al. 2012, SoPh, 275, 17
Li, X., Guo, F., Li, H., Stanier, A., & Kilian, P. 2019, ApJ, 884, 118
Li, Y., Qiu, J., & Ding, M. D. 2014, ApJ, 781, 120
Li, Y., Sun, X., Ding, M. D., Qiu, J., & Priest, E. R. 2017, ApJ, 835, 190
Lin, J., Li, J., Ko, Y.-K., & Raymond, J. C. 2009, ApJ, 693, 1666
Lin, R., Dennis, B., Hurford, G., et al. 2002, SoPh, 210, 3
Longcope, D. W. 2014, ApJ, 795, 10
López, F. M., Cremades, H., Balmaceda, L. A., Nuevo, F. A., & Vásquez, A. M. 2019, A&A, 627, A8
Loureiro, N. F., Schekochihin, A. A., College, K., & Cowley, S. C. 2007, PhPl, 14, 10
Lu, L., Feng, L., Warmuth, A., et al. 2022, ApJL, 924, L7
Lynch, B. J., Edmondson, J. K., Kazachenko, M. D., & Guidoni, S. E. 2016, ApJ, 826, 43
Machol, J. L., Eparvier, F. G., Viereck, R. A., et al. 2020, in The GOES-R Series, ed. S. J. Goodman et al. (Amsterdam: Elsevier), 233
Mathur, S., García, R. A., Régulo, C., et al. 2010, A&A, 511, A46
McLaughlin, J. A., Nakariakov, V. M., Dominique, M., Jelínek, P., & Takasao, S. 2018, SSRv, 214, 45
Meegan, C., Lichti, G., Bhat, P. N., et al. 2009, ApJ, 702, 791
Mei, Z., Shen, C., Wu, N., et al. 2012, MNRAS, 425, 2824
Mei, Z. X., Keppens, R., Roussev, I. I., & Lin, J. 2017, A& A, 604, L7
Miklenic, C. H., Veronig, A. M., Vršnak, B., & Hanslmeier, A. 2007, A&A, 461, 697
Moy, C. M., Seltzer, G. O., Rodbell, D. T., & Anderson, D. M. 2002, Natur, 420, 162
Müller, D., Marsden, R. G., St. Cyr, O. C., & Gilbert, H. R. 2013, SoPh, 285, 25
Müller, D., St. Cyr, O. C., Zouganelis, I., et al. 2020, A&A, 642, A1
Nakariakov, V. M., & Melnikov, V. F. 2009, SSRv, 149, 119
Naus, S. J., Qiu, J., DeVore, C. R., et al. 2022, ApJ, 926, 218
Neupert, W. M. 1968, ApJL, 153, L59
Ni, L., Kliem, B., Lin, J., & Wu, N. 2015, ApJ, 799, 79
Ohyama, M., & Shibata, K. 1998, ApJ, 499, 934
Parker, E. N. 1957, JGR, 62, 509
Parker, E. N. 1963, ApJS, 8, 177
Parker, J., & Longcope, D. 2017, ApJ, 847, 30
Pesnell, W. D., Thompson, B. J., & Chamberlin, P. C. 2012, SoPh, 275, 3
Petschek, H. E. 1964, NASSP, 50, 425
Pontin, D. I., & Priest, E. R. 2022, LRSP, 19, 1
Priest, E., & Forbes, T. 2002, A&ARv, 10, 313
Priest, E. R., & Longcope, D. W. 2017, SoPh, 292, 25
Pucci, F., Velli, M., & Tenerani, A. 2017, ApJ, 845, 25
Qiu, J., & Cheng, J. 2022, SoPh, 297, 80
Qiu, J., Liu, W.-J., & Longcope, D. W. 2012, ApJ, 752, 124
Richardson, I. G., & Cane, H. V. 2010, SoPh, 264, 189
Samtaney, R., Loureiro, N. F., Uzdensky, D. A., Schekochihin, A. A., & Cowley, S. C. 2009, PhRvL, 103, 105004
Shen, C., Lin, J., & Murphy, N. A. 2011, ApJ, 737, 14
Shibata, K., & Magara, T. 2011, LRSP, 8, 6
Shibata, K., & Tanuma, S. 2001, EP&S, 53, 473
Sturrock, P. A. 1966, Natur, 211, 695
Sun, X. 2013, arXiv:1309.2392
Sweet, P. A. 1958a, in Electromagnetic Phenomena in Cosmical Physics, ed. B. Lehnert (Cambridge : Cambridge Univ. Press), 123
Sweet, P. A. 1958b, NCim, 8, 188
Takahashi, T., Qiu, J., & Shibata, K. 2017, ApJ, 848, 102
Takasao, S., Asai, A., Isobe, H., & Shibata, K. 2012, ApJL, 745, L6
Thurgood, J. O., Pontin, D. I., & McLaughlin, J. A. 2017, ApJ, 844, 2
Torrence, C., & Compo, G. P. 1998, BAMS, 79, 61
Uzdensky, D. A., Loureiro, N. F., & Schekochihin, A. A. 2010, PhRvL, 105, 235002
Van Doorsselaere, T., Kupriyanova, E. G., & Yuan, D. 2016, SoPh, 291, 3143
Veronig, A. M., & Polanec, W. 2015, SoPh, 290, 2923
Wang, Y., Cheng, X., Ren, Z., & Ding, M. 2022, ApJL, 931, L32
Webster, P. J., Magaña, V. O., Palmer, T. N., et al. 1998, JGRC, 103, 14451
Wyper, P. F., & Pontin, D. I. 2021, ApJ, 920, 102